FINAL REPORT

PERFORMANCE STUDY OF A REPETITIVELY PULSED

TWO-STAGE PLASMA PROPULSION ENGINE

prepared for

NATIONAL AERONAUTICS AND SPACE ADMINISTRATION

by

B. Gorowitz, P. Gloersen, J. H. Rowe

November 20, 1963

CONTRACT NAS-3-2502

Project Manager
NASA-Lewis Research Center
Spacecraft Technology Division
Peter Ramins

GENERAL ELECTRIC CO.
Missile and Space Division
Space Sciences Laboratory
P.O. Box 8555
Philadelphia 1, Pennsylvania

NOTICE

This report was prepared as an account of Government sponsored work. Neither the United States, nor the National Aeronautics and Space Administration (NASA), nor any person acting on behalf of NASA:

A.) Makes any warranty or representation, expressed or implied, with respect to the accuracy, completeness, or usefulness of the information contained in this report, or that the use of any information, apparatus, method, or process disclosed in this report may not infringe privately owned rights; or

B.) Assumes any liabilities with respect to the use of, or for damages resulting from the use of any information, apparatus, method or process disclosed in this report.

As used above, "person acting on behalf of NASA" includes any employee or contractor of NASA, or employee of such contractor, to the extent that such employee or contractor of NASA, or employee of such contractor prepares, disseminates, or provides access to, any information pursuant to his employment or contract with NASA, or his employment with such contractor.

Requests for copies of this report
should be referred to:

National Aeronautics and Space Administration
Office of Scientific and Technical Information
Washington 25, D. C.
Attention: AFSS-A

TABLE OF CONTENTS

WHERE?

iii

LIST OF FIGURES

I. INTRODUCTION

This report describes an investigation of the performance of a two-stage, repetitively pulsed plasma engine. Although during the past year this study was conducted primarily under contract to the National Aeronautics and Space Administration, the basic design for this engine, preliminary tests of engine operation and the development of certain diagnostic techniques were conducted under company and other contract funding. In order to present in a logical manner the background for the various aspects of our experimental program, some of this auxiliary information will be included here. Up to the time of the present contract, a single-shot, single stage coaxial gun had been studied in considerable detail[1], leading to the concept of a two-stage repetitively pulsed engine. Although most of the subsequent effort had been applied toward ironing out operational difficulties while firing into a large test chamber, some data were obtained[2,3,4] on thrust as measured by a pendulum in the exhaust, collective velocities of the luminous species from streak camera and photomultiplier telescope records, determination of the luminous species present in the exhaust, and specific impulse of individual luminous species on one particular two-stage accelerator configuration. During the initial stages of this reporting period, studies of individual luminous species present and their velocities were continued, using accelerators which had undergone successive design modifications.

-1-

The chief objective of these modifications was to bring about

reliable operation of the accelerator for reasonably long times over a

wide range of power levels. Considerable success was achieved toward

this end and sufficient information was obtained to permit design and

construction of a refined version of the two-stage coaxial gun which was

used in the more extensive series of performance measurements (thrust,

efficiency, I_{sp}, etc.) to be discussed below.

In addition to this experimental effort, several theoretical approaches

to the study of the details of operation of the coaxial accelerator were

considered and one method was carried out to a logical stopping point.

The relationship of the analytically derived operating characteristics to

those found experimentally is examined and the data were utilized to predict

conditions of optimum engine operation.

2. THE ENGINE - GENERAL DESCRIPTION

A diagram of the circuit and electrode geometry of a typical two-

stage coaxial plasma engine is shown in Figure 1. The device consists of

two coaxial discharge chambers operated in tandem. The discharge of

the thrust-producing accelerator, represented in the circuit B of

Figure 1, is triggered by the injection of a burst of shock heated gas

from the relatively low power accelerator at the left through a series of

radial slots or holes. The electrical breakdown of this injector, which we

shall refer to as the first stage, is controlled by a standard ignitron switch.
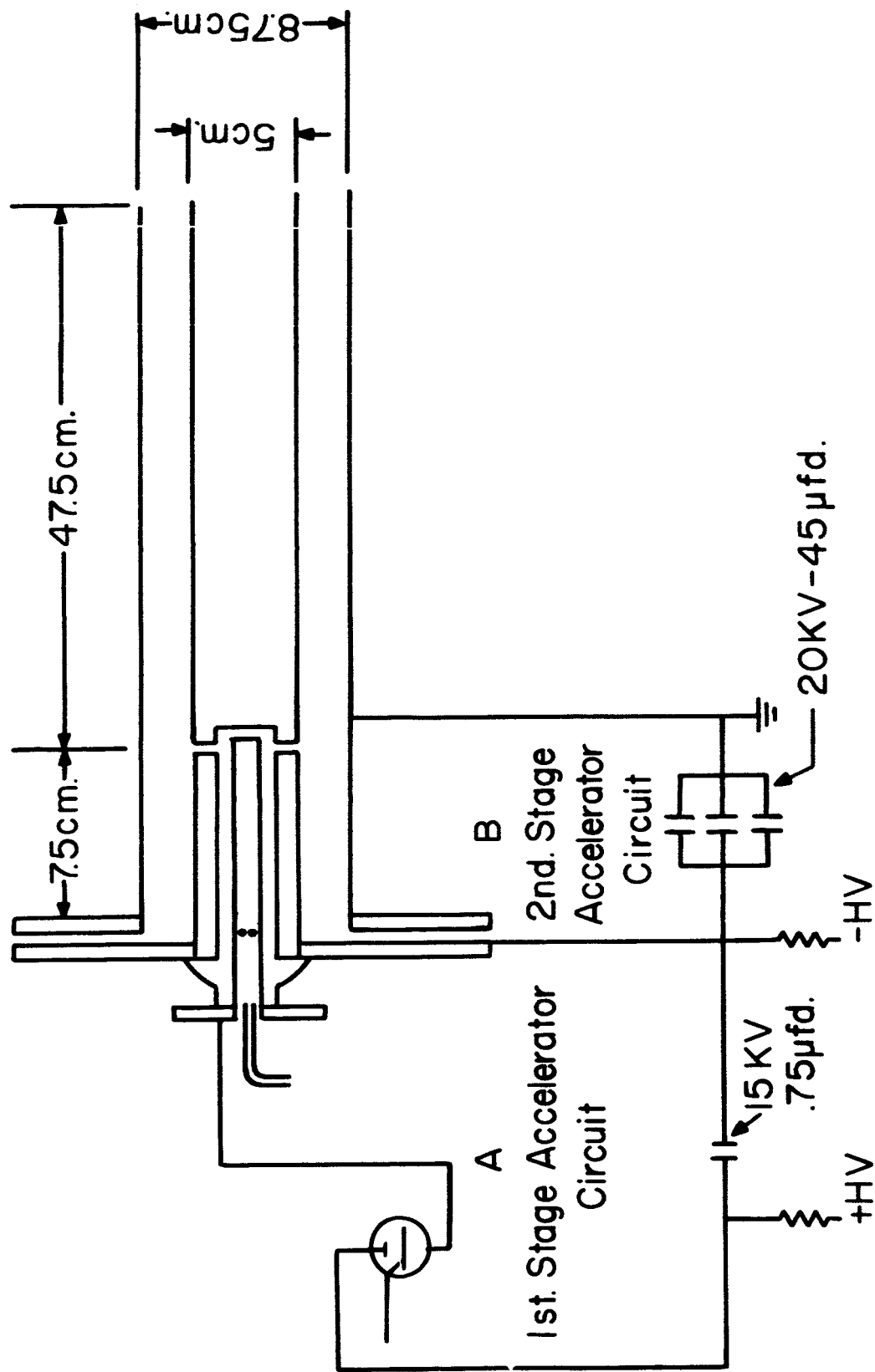
Figure 1. Circuit Diagram - Two Stage Coaxial Plasma Engine

The design of the engine is such as to provide an axial gradient in propellant density within the electrode structure as a result of flow toward the pumping system of the test chamber. With a continuous flow of propellant through the engine, the pressure in the second stage is low enough to prevent self-triggering, while that in the first stage is sufficiently high for reliable breakdown. The interstage pressure difference is accomplished primarily by adjusting the size of the interstage ports. A graph of a typical pressure distribution in the engine is shown in Figure 2. The values for second stage pressure were estimated from the pumping characteristics of the cylindrical gun geometry as well as those of the vacuum system. The plenum chamber and first stage pressures were measured with dial and thermocouple gauges respectively. The flow into the engine is controlled by a vacuum throttle valve and monitored with a capillary type flowmeter, calibrated with respect to back pressure, gas specific gravity, and operating temperature. A typical graph of vacuum chamber pressure versus mass flow is shown in Figure 3.

3. THE VACUUM FACILITY

The vacuum facility used for these studies consists of a 3 ft. diameter, 13 ft. long stainless steel chamber evacuated by three 32" oil diffusion pumps. These pumps are backed by a 2000 ℓ/sec oil diffusion ejector pump which is evacuated by a 200 cfm mechanical pump. The system achieves an ultimate pressure of 6 x 10^{-8} mm and has a maximum pumping speed of approximately 90,000 ℓ/sec in the range from 10^{-4} to 10^{-6} mm.
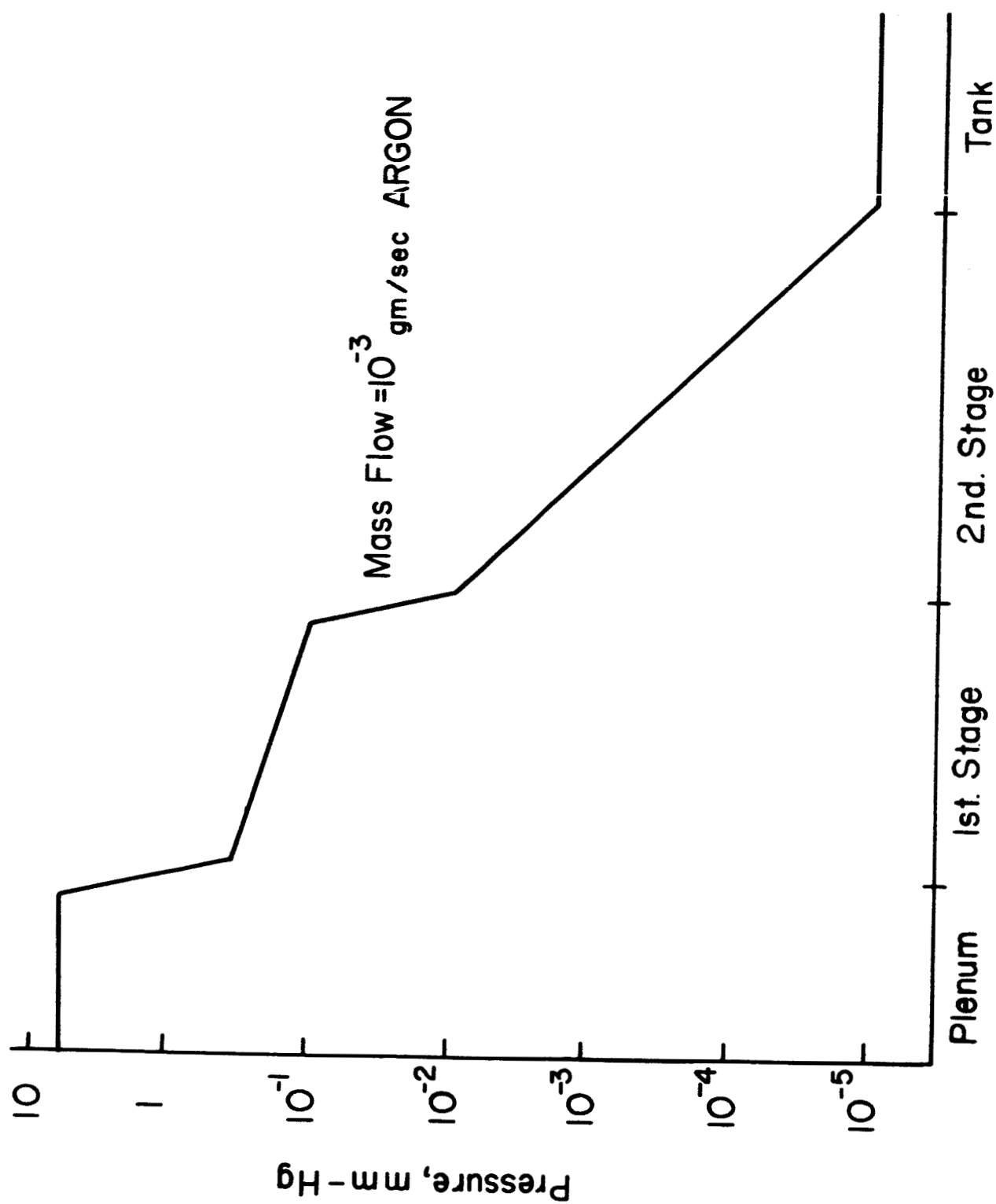
Figure 2. Typical Pressure Distribution in the Two-Stage Coaxial Gun
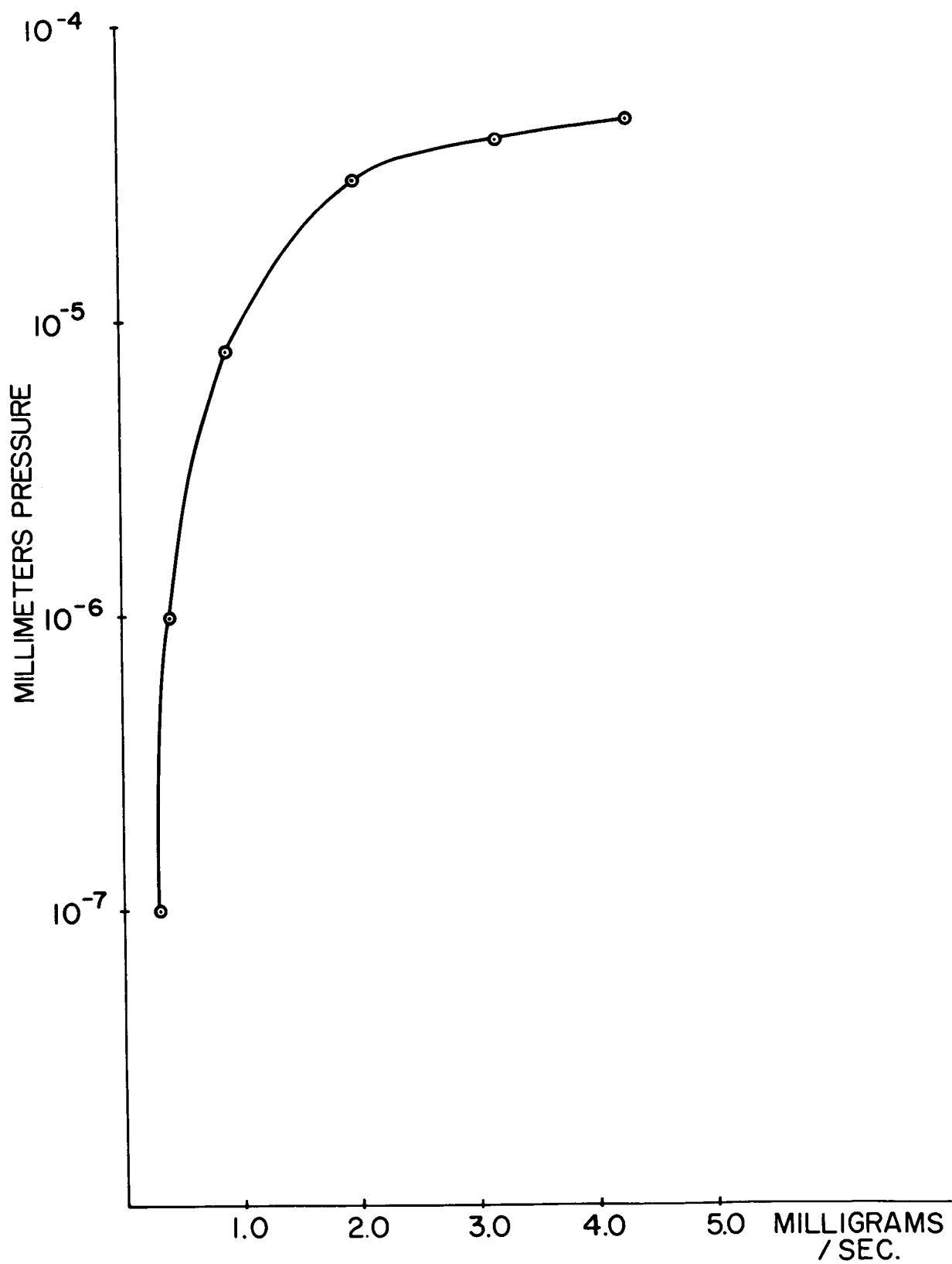
Figure 3. Chamber Pressure vs. Mass Flow of Nitrogen

A photograph of the facility as used for the first part of these studies is shown in Figure 4. At the left side of the photo may be seen one version of the two stage engine. The exhaust end of the engine is projected into the vacuum chamber through a sliding "O" ring seal arrangement.

After the first quarter of the contract period covered in this report, the system was modified to permit installation of an additional vacuum chamber in which engine systems including first and second stage energy storage capacitors and the first stage switch could be mounted on a thrust balance for tests under conditions approaching those of ultimate application. Photographs of the modified facility and addendum chamber are shown in Figures 5 and 6. To minimize the input of building and mechanical pump vibration to the thrust stand, various structural members of the vacuum system support were made with high rigidity, and vibration isolation was provided in other members where required. All gas, electrical, and coolant lines were flexible and properly oriented to avoid large null shifts in the thrust balance. The vacuum tanks were placed on air cushion servo leveler mounts which were used to maintain automatically the level of the entire assembly during closure and pumpdown and also to eliminate vibrations down to 7 cps. (Vibrations from the large mechanical pump and building were found to be in the range from 13-16 cps).

In order to facilitate convenient access to the engine for modification and instrumentation while permitting continuous operation of the oil diffusion pumps on the observation chamber, a 30" diameter full opening
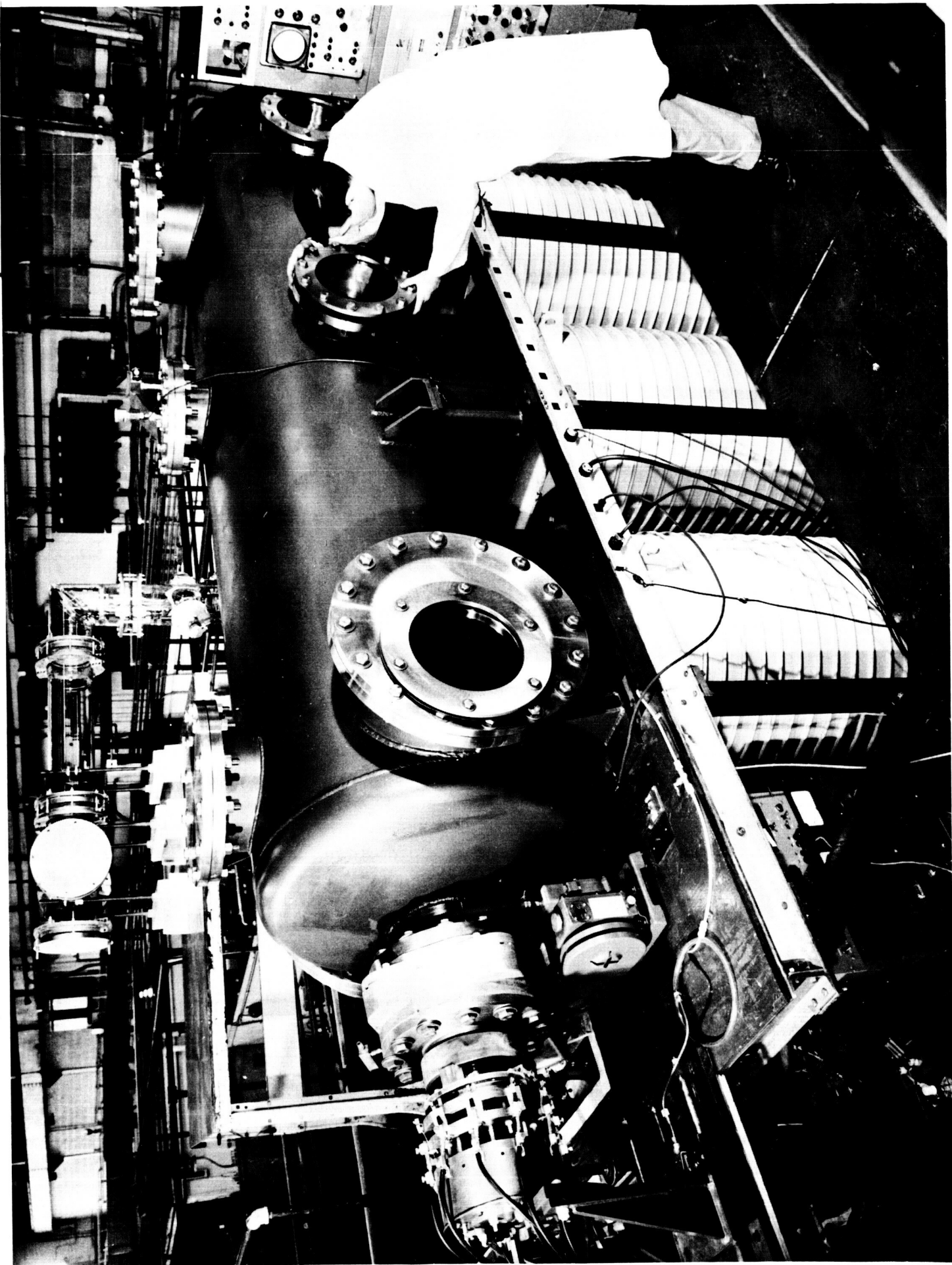
Fig. 4. Initial Plasma Engine Test Facility.
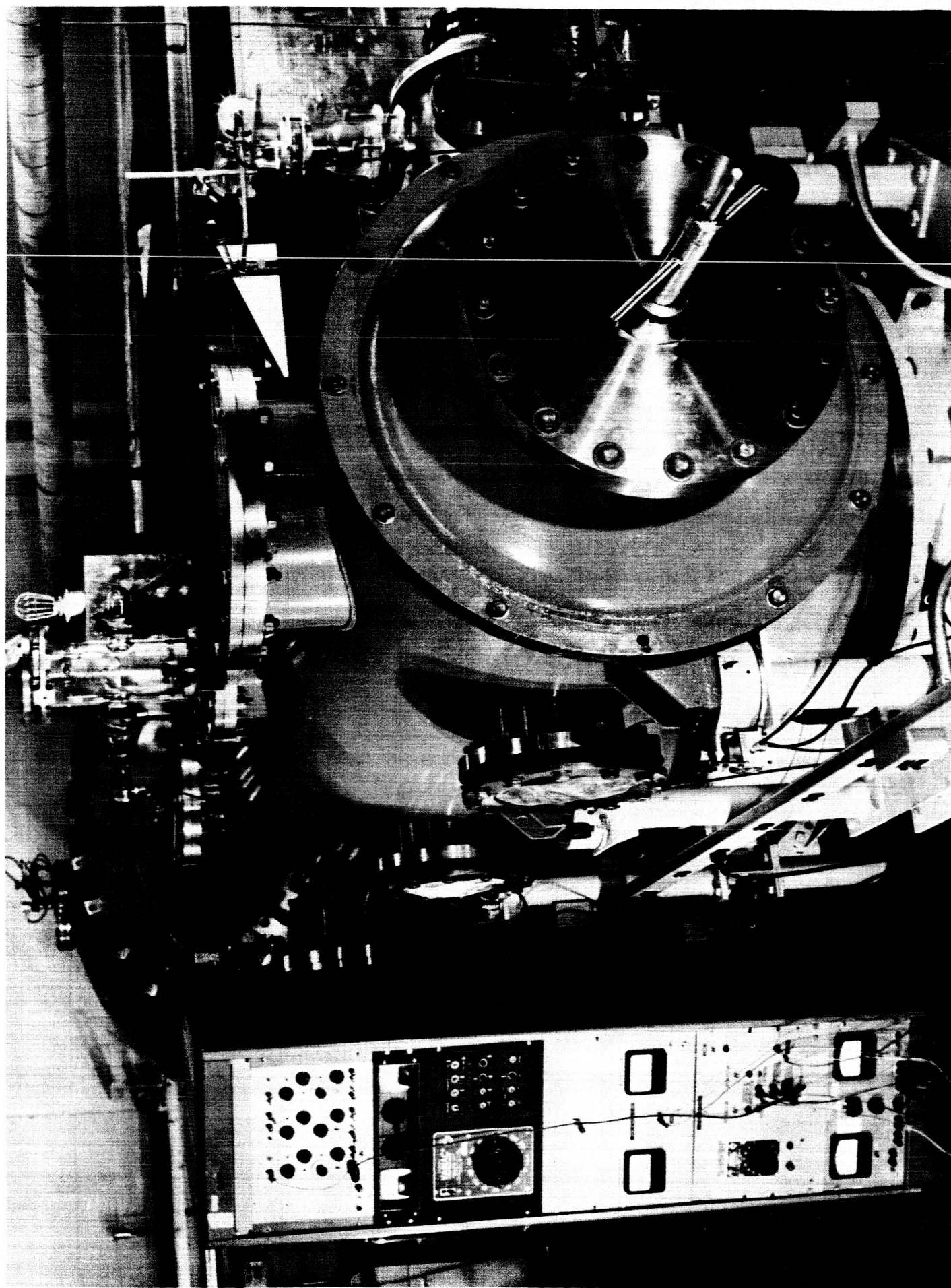
Fig. 5. Modified Plasma Engine Test Facility.
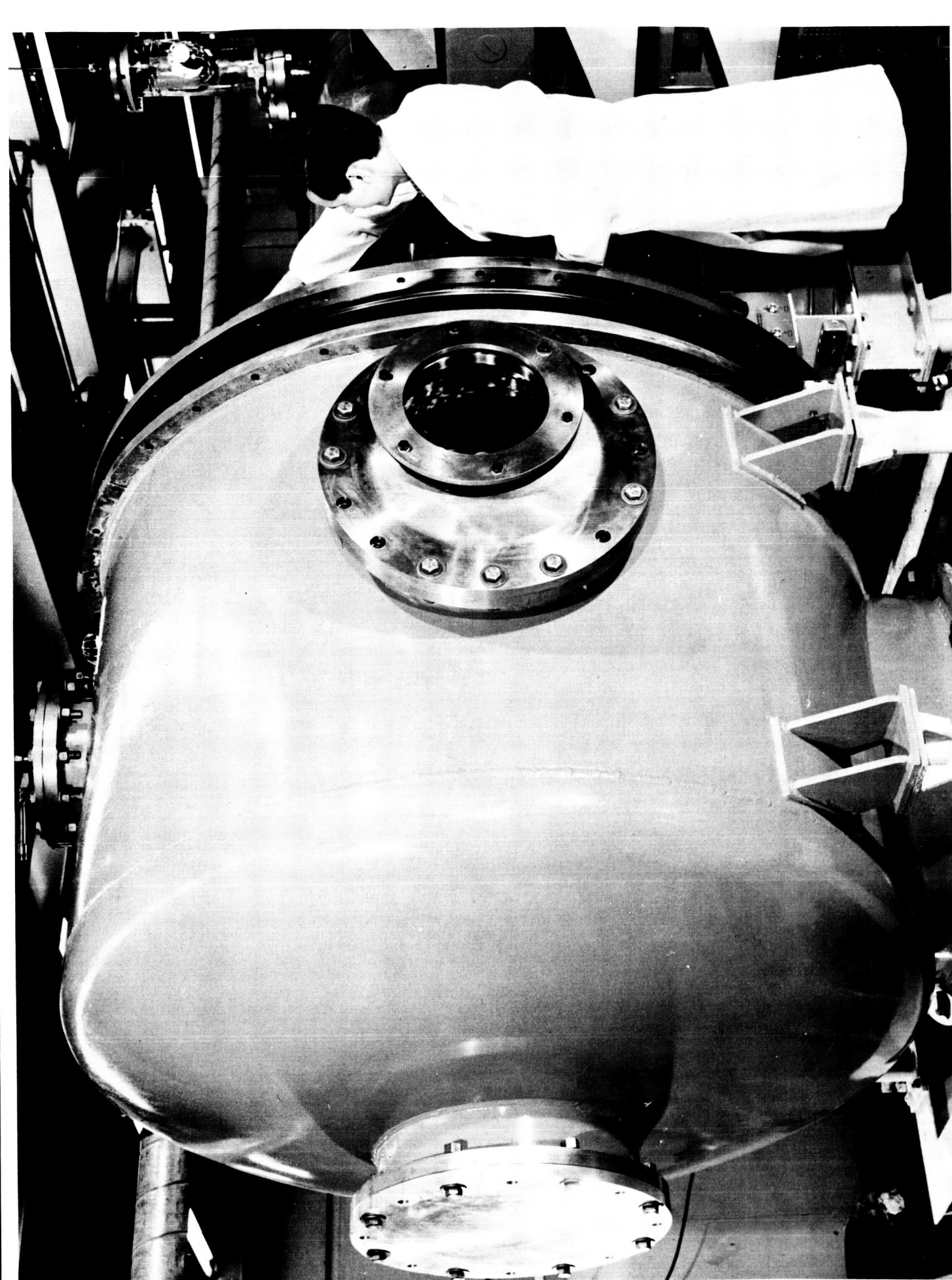
Fig. 6. Addendum Tank - Thrust Stand and Engine Housing.

bell-shaped valve was provided in the interchamber opening. The valve allows the engine to remain in a position where it protrudes into the observation chamber from the auxiliary chamber while the two sections are isolated from each other. When open, the valve is moved to the far end of the vacuum chamber on a carriage and track arrangement.

4. THE ELECTRICAL FACILITY

A block diagram of the electrical components associated with the operation of the two-stage engine is shown in **Figure 7.**

High voltage, vacuum-tight electrical lead-throughs mounted on the pumping plate of the chamber containing the engine and thrust balance provide for the transfer of power to the first and second stage energy storage capacitors and transmittal of trigger signals for the first stage ignitron switch. The entire test facility was properly interlocked to prevent accidental access to the engine prior to removal of dangerous voltages after chamber pressurization.

5. ENGINE PERFORMANCE MEASUREMENT TECHNIQUES

That portion of the study of the performance of the two-stage plasma engine conducted during the past year has consisted primarily of the following measurements:

    A. Engine thrust
    B. Plasma kinetic energy
    C. Plasma species
    D. Plasma specie time-of-flight
    E. Input mass flow rate
    F. Discharge current and voltage transients
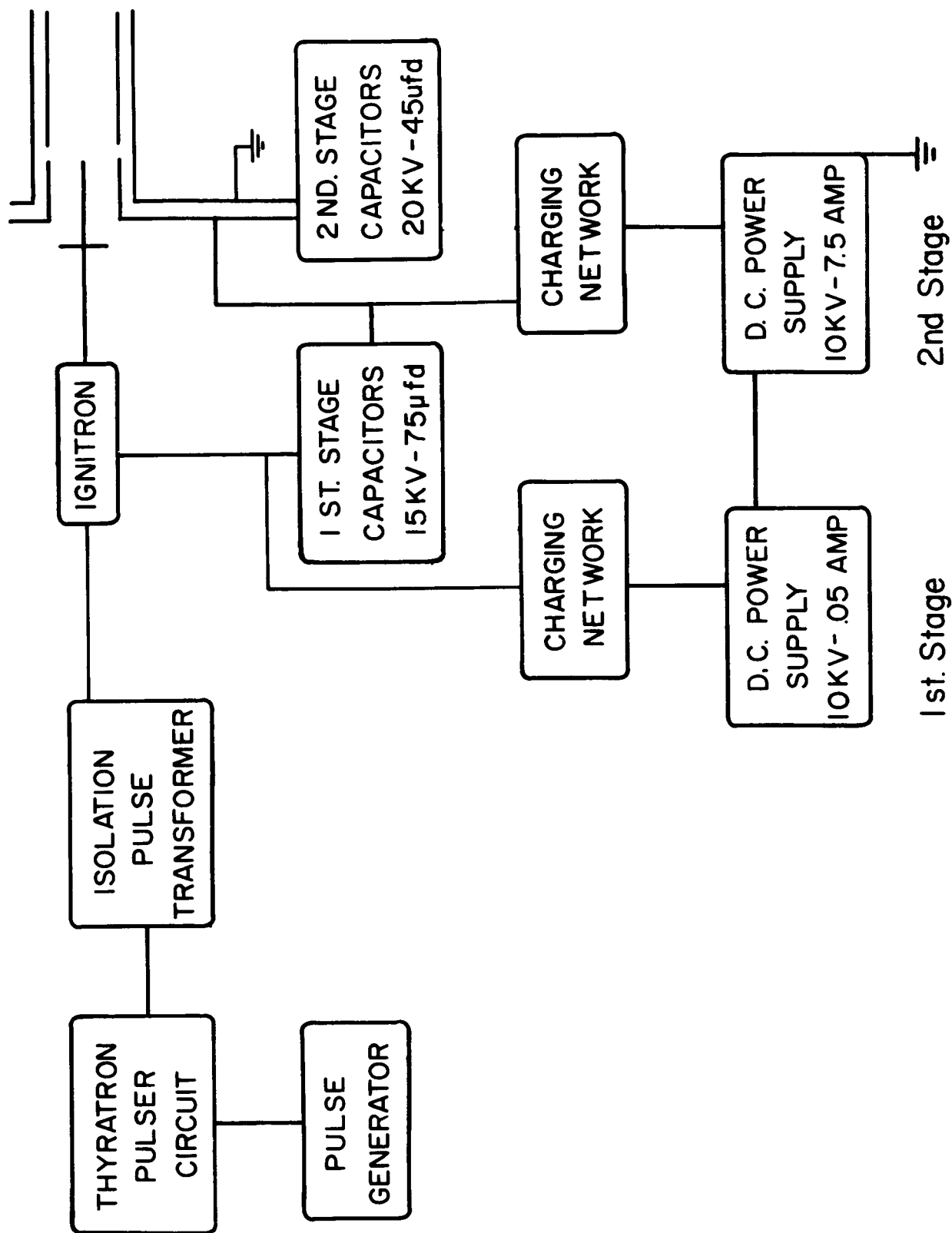
Figure 7. Electrical Components - Two-Stage Coaxial Plasma Engine

The development of facilities and the refinement of techniques associated with these measurements and their application constituted a major portion of our experimental program and as such are described in some detail below, along with comments as to the reliability of each.

These measurements have been used to obtain the vital operating parameters of the two-stage coaxial gun, namely, the thrust/power ratio, the specific impulse, the energy efficiency, and the mass utilization. The validity of such application of the measurements also will be examined in detail later.

5.1 Engine Thrust

For various reasons, which shall not be discussed again here, the validity of the use of the ballistic pendulum for the measurement of engine thrust has long been subject to question by the majority of those involved in electrical propulsion research.

Since the thrust measurements quoted here were obtained by measuring the reactive force produced by the gun and energy storage system mounted on a sensitive thrust balance, the average thrusts so obtained can hardly be disputed on the basis of principle, providing that possible spurious effects due to stray magnetic fields or other improper thrust balance operation are eliminated or properly taken into account. The thrust balance described here was implemented not only to obtain a more reliable method for measuring thrust but also to make

possible the calibration of pendula which might be more conveniently

used in other phases of the engine testing program.

5.1.1 General Description of the Thrust Balance

The thrust balance used here is of the loaded column type[5,6].

It supported all of the major components of the engine, including the

first and second stage capacitors and the two-stage coaxial plasma

accelerator, and was designed to easily accommodate a total loading

up to 440 Kg., representing primarily the weight of the engine system,

the engine mounting rack, and the necessary counterweights. In spite

of this relatively large mass, the thrust balance is capable of providing

a measurable reaction to thrusts in the micronewton range. The

columns utilized in our assembly consisted of three rectangular flexure

plates mounted between a movable engine mounting rack and a stationary

lower frame, and loaded to nearly their critical buckling point.

Equations for deflection and period of vibration were developed as

a function of the flexure plate geometry and the applied buckling (P = mg)

and thrust (F) forces by treating the flexure plates as cantilever beams

with axial and lateral end loading. The basis for the analysis was the

general differential equation

$$EI \frac{d^2 y}{dx^2} = M_x = F(L - x) - M_o + Py(x) \tag{5.1}$$

which may be developed by expressing the stress in a beam as a function

of deflection and radius of curvature, the term $\frac{d^2 y}{dx^2}$ being equal to the

-14-

inverse of radius of curvature. In the above equation, M_x is the

local moment in the beam, E is the material modulus of elasticity,

I is the beam moment of inertia, y is the beam deflection transverse

to the axis direction, x, L is the beam length, and M_o is the pure

torque applied by thrust stand constraints to produce an "S"-shaped

flexure. This is illustrated in Figure 8. The solution of this equation

for the case of a homogenous beam of constant section I and length L

under a buckling load P and a thrust load F is obtained as follows:

Note that

$$M_x'' = Py'' = \frac{P}{EI} M_x \tag{5.2}$$

The general solution for this equation is

$$M_x = C_1 \sin\left(\frac{P}{EI}\right)^{1/2} x + C_2 \cos\left(\frac{P}{EI}\right)^{1/2} x \tag{5.3}$$

By comparing M_x and M_x' obtained from equations (5.1) and (5.3)

at the boundary x = 0, and by noting that y'' and hence M''_x (obtained

again from Equation (5.3) is zero at $x \cong L/2$, we obtain values of C_1,

C_2, and M_o, so that solving Equation (5.1) for y and substituting in the

values for M_x and M_o, we obtain:

$$y(x) = \frac{-F}{P}\left\{\left(\frac{EI}{P}\right)^{1/2}\left[\tan\left\langle\left(\frac{P}{EI}\right)^{1/2}\frac{x}{2}\right\rangle\left(1 - \cos\left(\frac{P}{EI}\right)^{1/2} x\right) + \sin\left(\frac{P}{EI}\right)^{1/2} x\right] - x\right\} \tag{5.4}$$

The deflection at the end of the flexure is obtained by setting x = L.
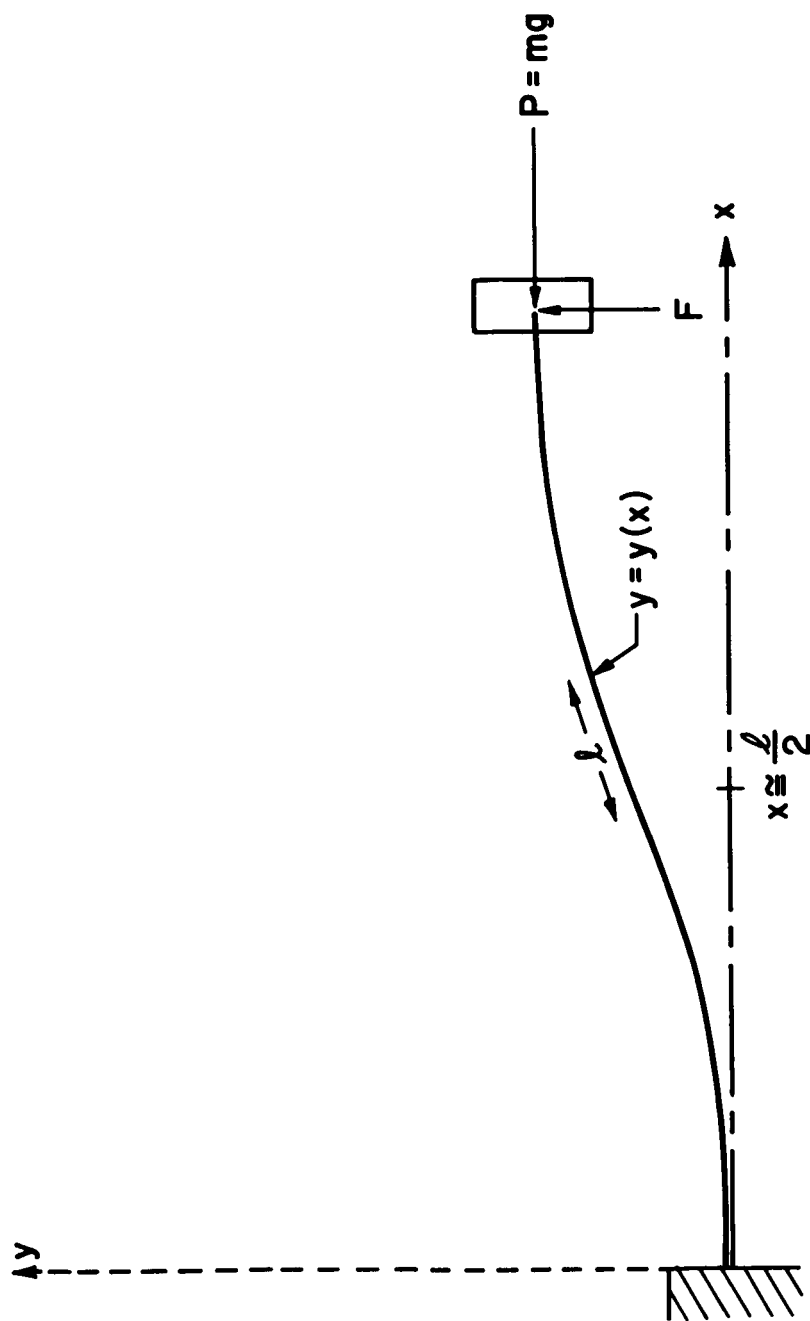
Figure 8. Bending of the Thrust Balance Flexure

The critical buckling point ($y \to \infty$) occurs when $\tan \langle \rangle \to \infty$, or

$$P = mg = \frac{\pi^2}{L^2} EI \tag{5.5}$$

Equation (5.4) may also be written

$$F = m\ddot{y} = -P \{ \}^{-1} y(L)$$

to express the motion of the end of the flexure if F suddenly drops to zero. The period of this motion is given by

$$T = 2\pi \left(\frac{y(L)}{\ddot{y}} \right)^{1/2}$$

or

$$T = \frac{2\pi}{g^{1/2}} \left\{ \left(\frac{EI}{mg} \right)^{1/2} \left[\tan \left\langle \left(\frac{mg}{EI} \right)^{1/2} \frac{L}{2} \right\rangle \left(1 - \cos \left(\frac{mg}{EI} \right)^{1/2} L \right) + \sin \left(\frac{mg}{EI} \right)^{1/2} L \right] - L \right\}^{1/2}$$

Figure 9 shows the thrust balance sensitivity in terms of deflection per unit thrust as a function of percent critical load based on the flexure supports used during the major portion of the data gathering period. Sensitivities as high as 0.5 mils per millinewton have been obtained, but the major portion of testing has been accomplished at .045 mils per millinewton. This represents a vertical loading of 97.5% critical. The observed period of the thrust balance was 3 seconds. This value corresponds to a calculated period of 3.2 seconds for 97.5% critical load.

An expression convenient to use in altering vertical flexure dimensions in the event a given load on the thrust balance is not sufficiently near the

CALCULATED THRUST STAND SENSITIVITY
(DEFLECTION/THRUST)
VS.
PERCENT CRITICAL LOADING
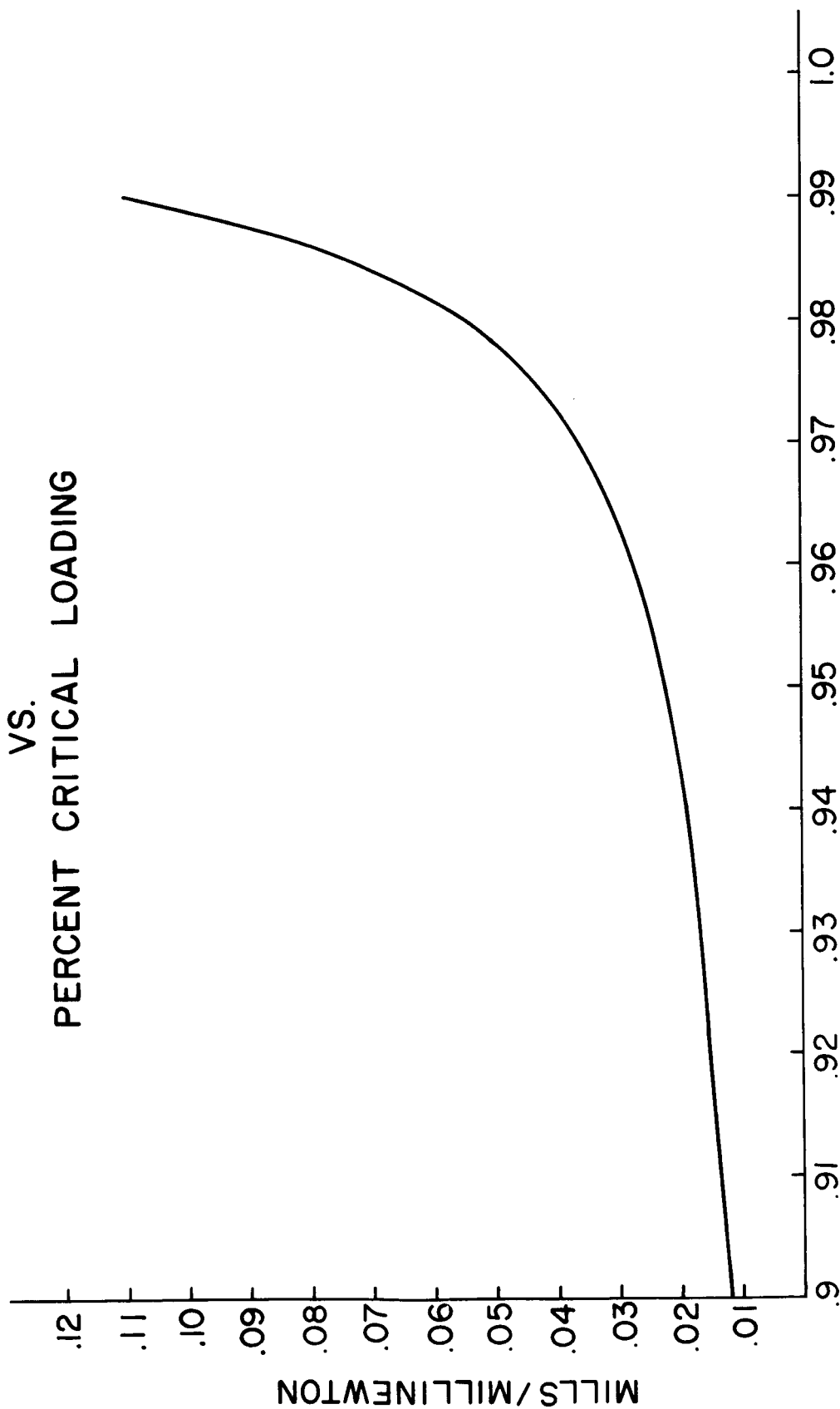
Figure 9. Calculated Thrust Stand Sensitivity (Deflection/Thrust)
vs. Percent Critical Loading

critical buckling point is obtained by a first order expansion of

Equation (5.4) about the critical point. The result is:

$$y(L) = \frac{2FE^{1/2} I_o}{\pi (mg)^{3/2} (I - I_o)^{1/2}}$$

(5.7)

5.1.2 Details of the Thrust Balance and Instrumentation

A photograph of the thrust balance assembly mounted on the

interchamber plate is shown in Figure 10. The capacitor rack, lower

frame and flexure plates are constructed of a 31% Nickel alloy (Super

Invar) in order to minimize any drifts which might occur due to thermal

expansion transients. The main support frame is made of 304 stainless

steel.

Gross correction of thrust balance level is obtained by means of

screw jacks between the lower frame and the main support frame. The

main support frame, in turn, may be adjusted from outside the vacuum

system by a differential screw passing through a vacuum seal in the

interchamber plate. This permits fine adjustment of the thrust balance

null point without opening the vacuum chamber. Equal loading of the

flexure plates is accomplished initially by adding counterweights to a

pan affixed to the capacitor frame. Fine balance is subsequently made

by sliding additional weights in two orthogonal directions in the horizontal

plane.

The movement of the thrust balance under load is detected by a

linear variable differential transformer. The transformer core

-19-
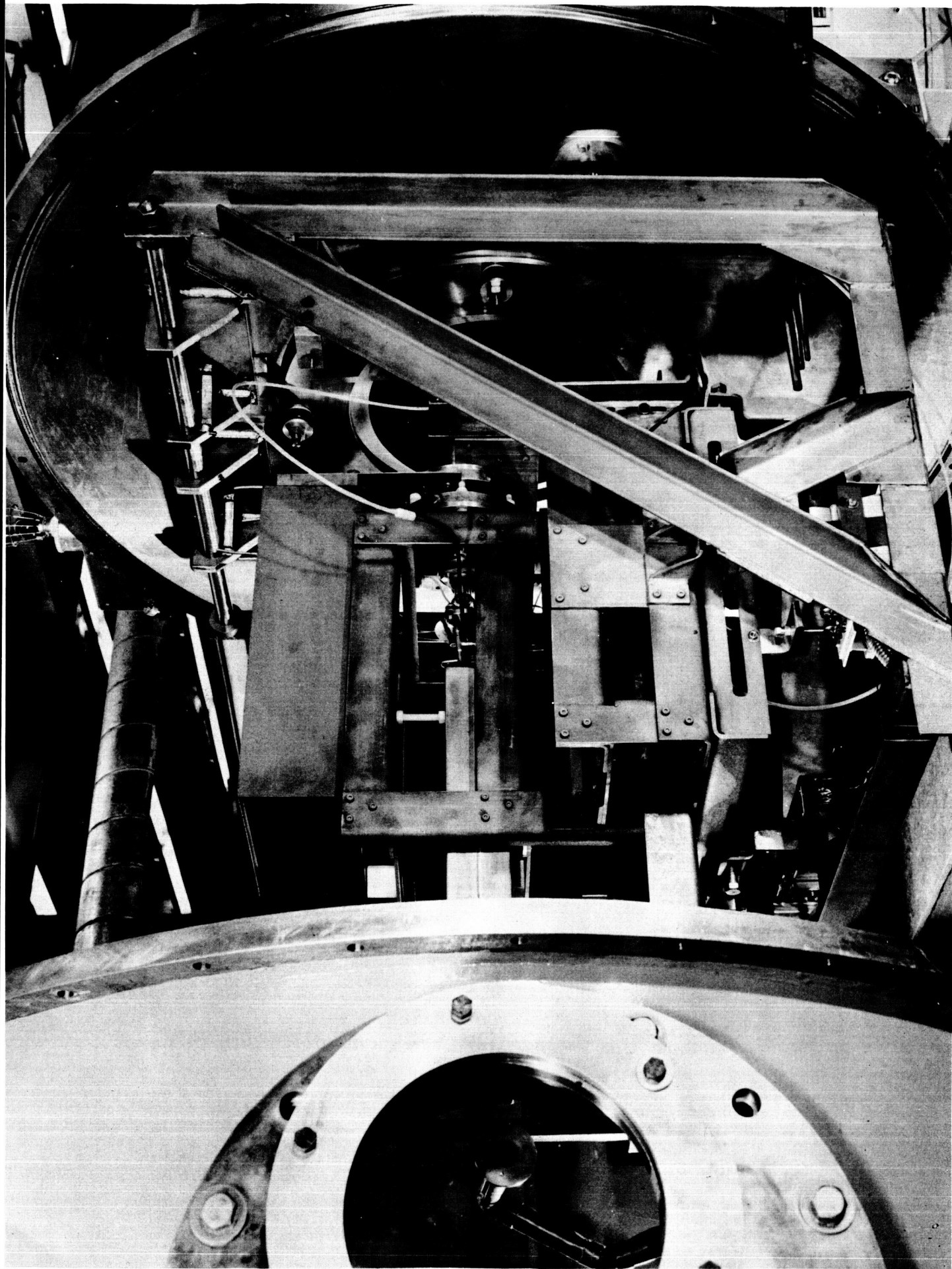
Fig. 10 Thrust Balance Assembly.

is mounted on the moving portion of the balance and is mechanically independent of a coil assembly mounted on the stationary portion. Under thrust conditions producing motion beyond the linear range of the transformer (.01"), a solenoid is used to react the thrust and return the balance to the null point. The solenoid current required to produce a balance null is calibrated to read thrust directly. The calibrating element is a thin steel reed with a known force/deflection ratio, cantilevered from the moving portion of the thrust balance. Its free end is statically deflected from outside the vacuum system by a hand operated screw arrangement passing through a vacuum seal. Calibration of the thrust balance was made before and after thrust runs.

5.1.3 Measurements

Operation of the thrust balance during this period has been in the thrust range below 45 millinewtons. This represents a deflection of the balance of less than 2 mils and is within the linear range of both the balance itself and the differential transformer. Thrust readings,therefore, have been made by recording the deflection directly on a strip chart recorder without use of the null correcting solenoid.

Figure 11 shows a chart record for a typical thrust run. The reed calibration prior to the run is shown in Figure 12. Note that during the run, there was a slight shift in the balance null point, though the initial average deflection and final average deflection were the same. This

-21-

Voltage - 12 KV
Capacitance - 45 ufd
Firing Rate - 2 cps
Propellant - N_2
Chamber Pressure - 4×10^{-6} mm
Thrust - 34.2 millinewtons
Chart Speed - 2"/minute

Thrust Calibration

10 div = 17 millinewtons
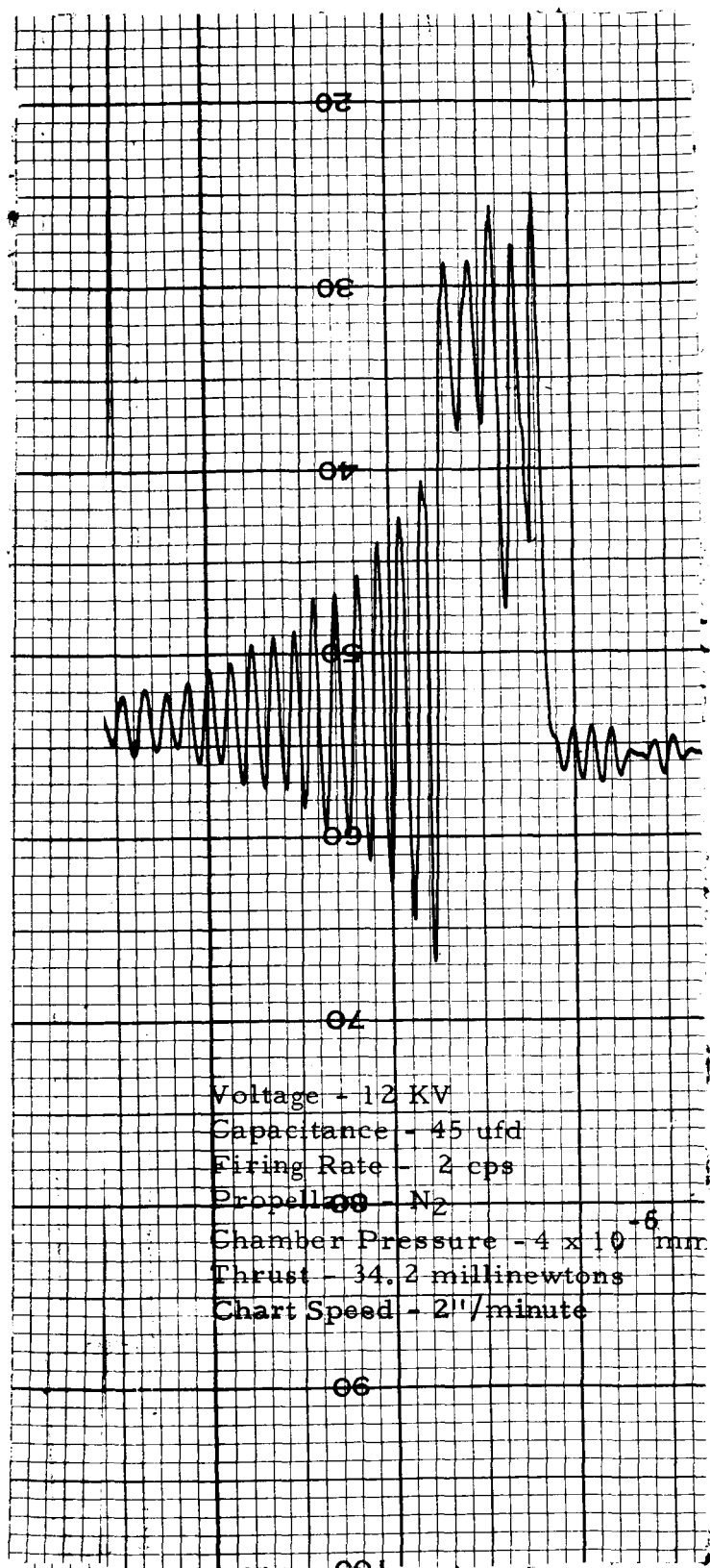
Figure. 11. Thrust Run Record
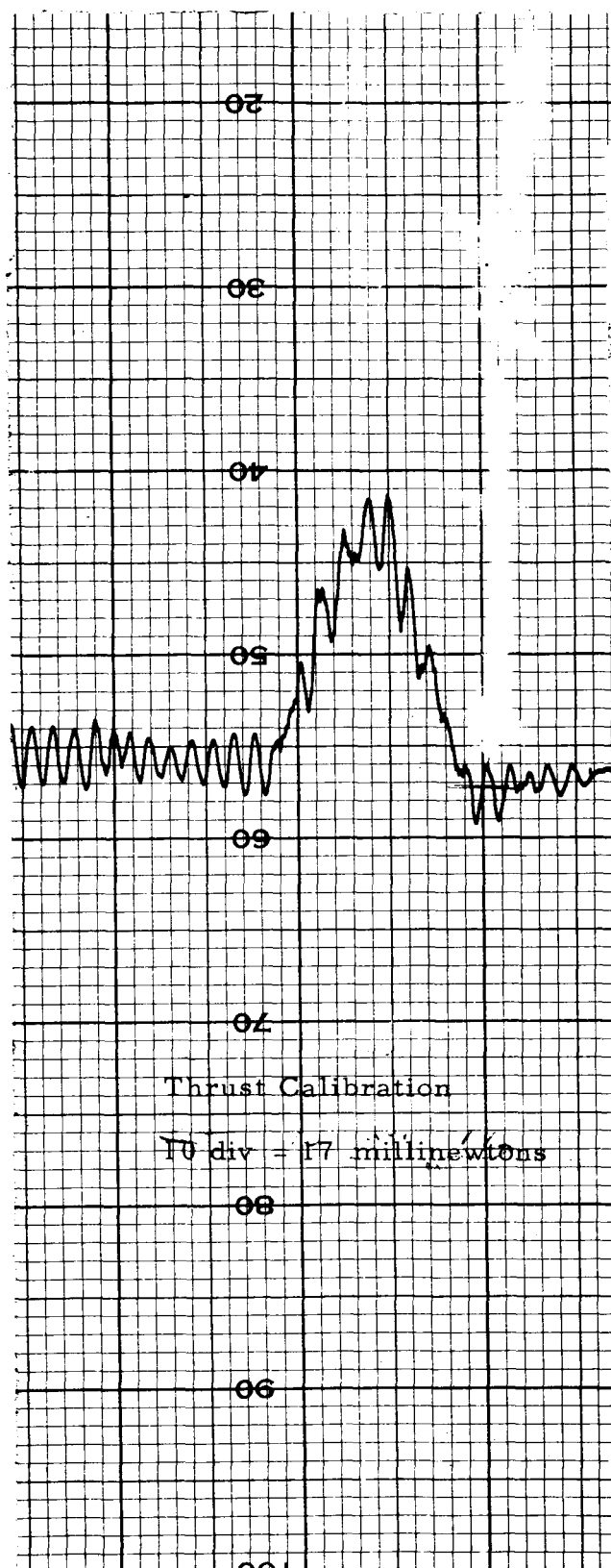
Figure 12. Thrust Balance Calibration

-22-

shift is apparently due to a thermal effect since the balance returns to its original position after a short cooling period. This shift does not affect the accuracy of the readings since continuous monitoring allows the extent of the shift to be observed during the run and the initial and final deflection to be compared. (This will also be true with operation of the nulling solenoid, since final position of the thrust balance can always be compared with initial position and correction made in the solenoid current reading.)

The thrust balance has been operated with capacitor and electrode oil cooling lines attached. These lines are long flexible metal hose arranged vertically to minimize the oil flow effect on the thrust stand. Sensitivity is not affected by connection of these cooling lines nor by the flowing oil inside the lines. However, the null position does shift slightly when the cooling oil circulating pump is started, indicating a steady component of axial load on the thrust balance. Undoubtedly, this can be corrected by rearrangement of the line connections. A change in density of the circulating oil also has an effect. This is indicated by a thrust balance drift during extended engine runs with the oil pump in operation, when oil density is changed by a temperature rise in the oil. Consequently, all thrust runs to date have been made with the circulating pump off.

In order to determine the effect of stray magnetic fields on thrust readings, a number of runs were made by shorting the second stage electrode at the exit end through an ignitron and pulsing the engine

without gas flow. Under these conditions, no deflection of the thrust balance was detected, indicating an absence of magnetic field effect on the readings.

5.2 Plasma Kinetic Energy

Another measuring technique considered satisfactorily reliable at this time is the determination of the directed plasma energy in the exhaust stream by small or large calorimeters. The measurements tend to be conservative from the standpoint of quoting thrust efficiency, when taken under the proper conditions, because the collecting efficiency of the calorimeter is probably less than unity, for reasons discussed later. Caution must be taken to exclude from the calorimeter strong, rapidly changing magnetic fields. Another precaution is to determine the extent to which the plasma spreads upon leaving the gun (an indication of the ratio of thermal to directed energy) and to both collect all the plasma and subtract from the measured values the thermal portion of the energy, if the latter is an important fraction of the total energy.

Calorimeter targets were used for the determination of the directed plasma energy in the exhaust stream. In the predominant number of experiments performed during the period covered by this report, the calorimeter consisted of a 5"long copper cone with a base diameter of 9-1/2" and a copper constantan thermocouple affixed to the apex of the cone. The cone was suspended from an overhead port in the

-24-

observation tank at a position 6" from the exhaust end of the engine.
The weight of the cone was 150 grams. In typical runs, the engine
was pulsed 10 to 20 times at 1 shot per second before a reading of
calorimeter temperature increase was made. With the reference
junction at 0° C, the thermocouple output was measured on a strip
chart recorder with full scale adjustable from 0 to 10 millivolts. The
recorder was calibrated against an auxiliary potentiometer-standard
cell arrangement. In order to prevent any possible flow of discharge
current through the thermocouple wires, the calorimeter was isolated
from the recorder input by a high voltage switch which was closed only
after the completion of the run, after the engine capacitors were fully
shorted to ground.

A typical strip chart record is shown in Figure 13. The peak
temperature indicated by the record represents the temperature of
only a portion of the calorimeter in the vicinity of its apex. The
temperature is distributed evenly in the calorimeter only after a
sufficiently long waiting period after pulse heating it. In the meantime,
calorimeter energy is being radiated to the cooler surfaces of the
surrounding test chamber. It is necessary, therefore, to devise an
appropriate extrapolation procedure for determining an effective
calorimeter energy at the time of engine cut-off. An emperically
determined extrapolating curve was generated by the following technique:
While in the measuring position, the calorimeter was heated uniformly

-25-

x49.0°C

$\Delta T = 20.8°$
$\Delta T/Shot = 4.16°$

CHART
SPEED
.5IN./MIN.

28.2° C
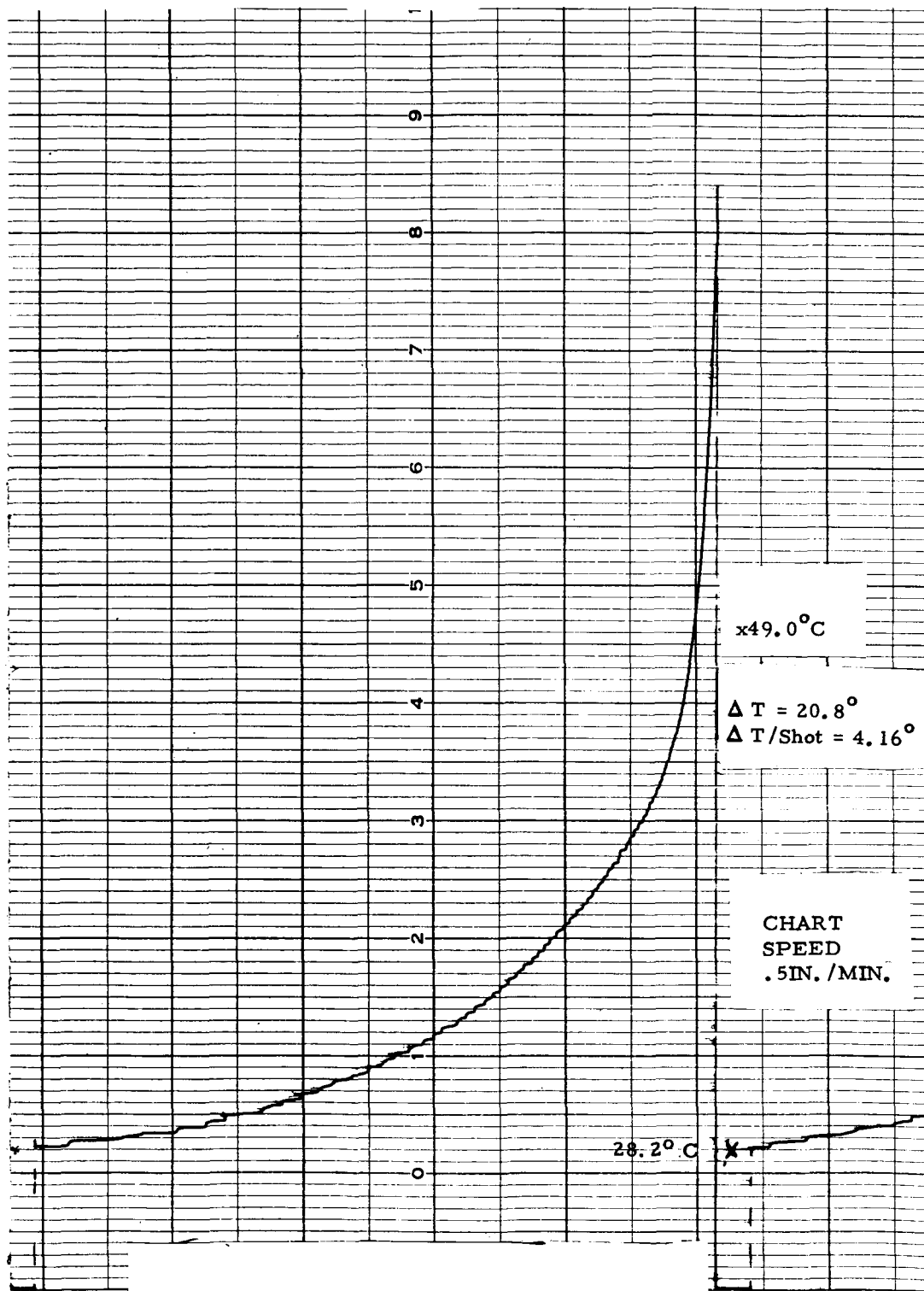
Figure 13. Calorimeter Cooling After Engine
Operation - 5 Shots

-26-

by means of an infrared lamp aimed at the calorimeter through a window in the test chamber until a temperature comparable to that generated by the engine exhaust stream was obtained. The calorimeter temperature was rapidly cycled, with small amplitudes, about that temperature for a time sufficiently long to insure a uniform distribution of heat. The calorimeter was then allowed to cool, and the resulting recorded temperature decay curve was superimposed on engine data records obtained after operating the engine for short periods of time to obtain extrapolated temperatures representing the energy in the calorimeter at engine cutoff. A sample curve obtained by infrared heating is shown in Figure 14. It was observed that changing surface characteristics of the calorimeter altered the shape of the cooling curves, so that it was necessary periodically to redetermine the cooling patterns.

Possible losses due to unequal radiative cooling of the apex compared to the rest of the cone during redistribution of heat, or losses received in vaporizing vacuum chamber oil, carbonized oil, or other materials from the surface of the calorimeter were not taken into account. The effect of convective cooling by the propellant which was continuously flowing from the engine has been investigated and found to be too small to measure in the arrangement used. These effects, coupled with the
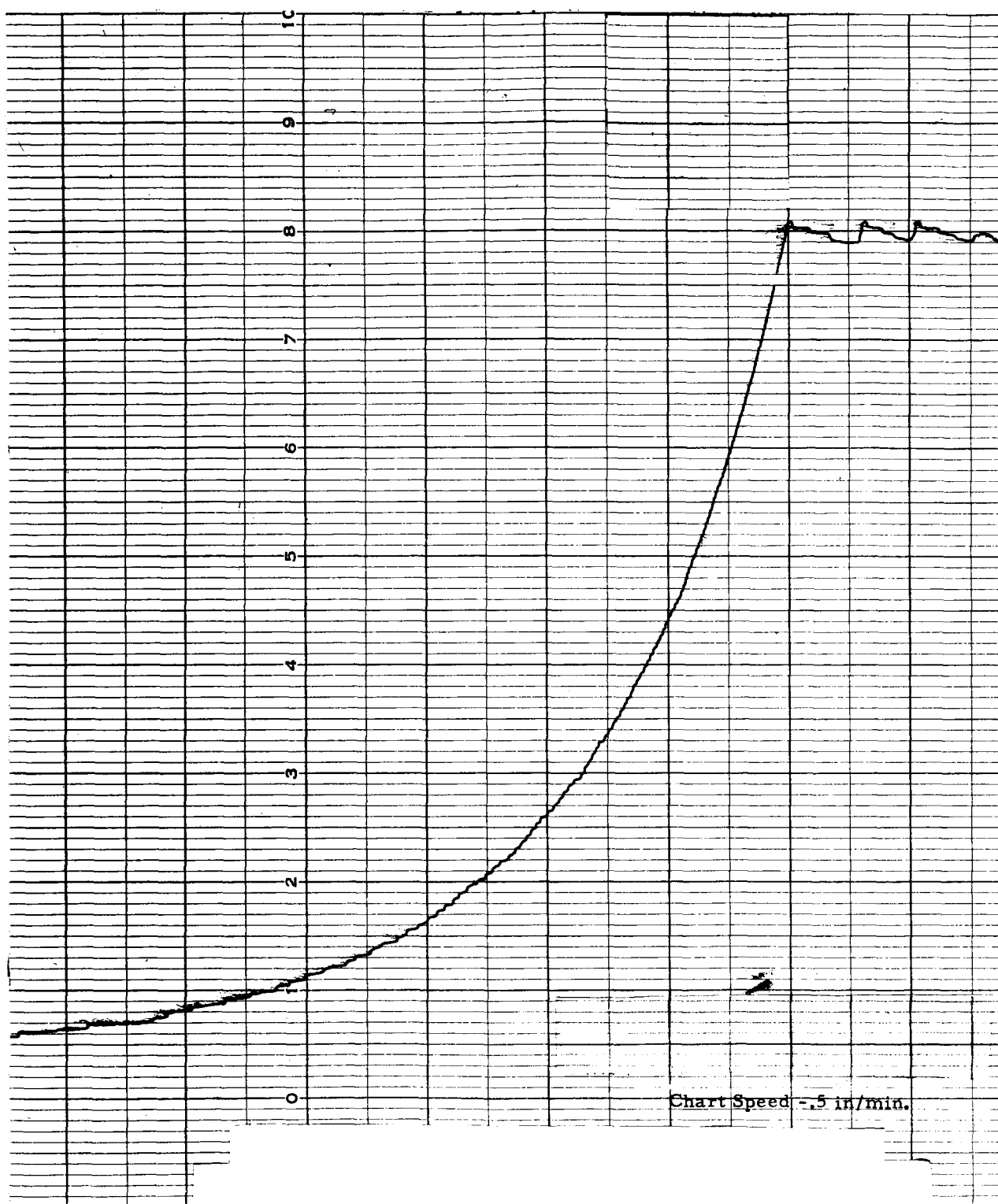
Figure 14. Cooling of Calorimeter from Equilibrium
after Heating with Infrared Lamp.

Chart Speed - .5 in/min.

less-than-perfect collection of the plasma by the calorimeter, all tend to render the readings thus obtained on the conservative side. Factors which might tend to increase the reading include eddy current heating due to rapidly changing magnetic fields at the calorimeter (which are deemed negligible in this arrangement since the luminous plasma appears at the gun muzzle well after the first cycle of current), radiation transfer from the inner electrode (which was small since the electrodes were kept cool), and plasma heating by the thermal portion of the plasma energy. As will be shown, measurements of plasma spreading indicate that this latter contribution is relatively small.

In addition to the conical calorimeter mentioned above, a 4" diameter, 1" long cylindrical cup, was used to provide additional plasma kinetic energy data as well as to give an indication of plasma exhaust stream spreading. This was accomplished by moving the smaller calorimeter through the cross-section of the plasma exhaust.

An appropriate summing procedure was devised, and it was found that the total plasma energy so obtained agreed with the single reading determination from the larger calorimeter to within 5%. Measurements obtained with the smaller calorimeter at various points in the stream indicated that approximately 50% of the energy appeared in a conical half angle of less than 5° with respect to the muzzle while almost all of the remaining energy in the stream was accounted for within a 22° half angle.

5.3 Plasma Species

5.3.1 Emission Spectroscopy

A 1.5 meter Bausch and Lomb spectrograph was initially used to obtain spectrograms of the plasma luminosity at the muzzle of the engine. Because of the low level of luminosity, exposure times as long as 20 minutes were required while the engine was fired at a repetition rate of 10 cps.

In order to improve the signal-to-noise ratio, the photographic technique was replaced by a more sensitive photoelectric spectral mapping technique. The plasma luminosity at the breech and at the muzzle of the accelerator was examined with a JACO .5 meter Ebert scanning monochromator equipped with a photomultiplier detector and associated balanced electrometer amplifier. The portion of the spectrum from 3000 to 4500 A was scanned at a rate of 20A/min while the engine was at 10 cps. Because of the increased sensitivity, the number of specie lines observed was far greater than that observed photographically, when the photomultiplier was operated either continuously or gated in synchronization with the engine.

5.3.2 Vacuum Ultraviolet Spectroscopy

A technique for future use in observing non-luminous plasma species in the plasma exhaust stream was largely implemented in this period, primarily with the support of another contract. A drawing of the optical arrangement to be used is shown in Figure 15. All of the vacuum optical path components have been fabricated and assembled, including required
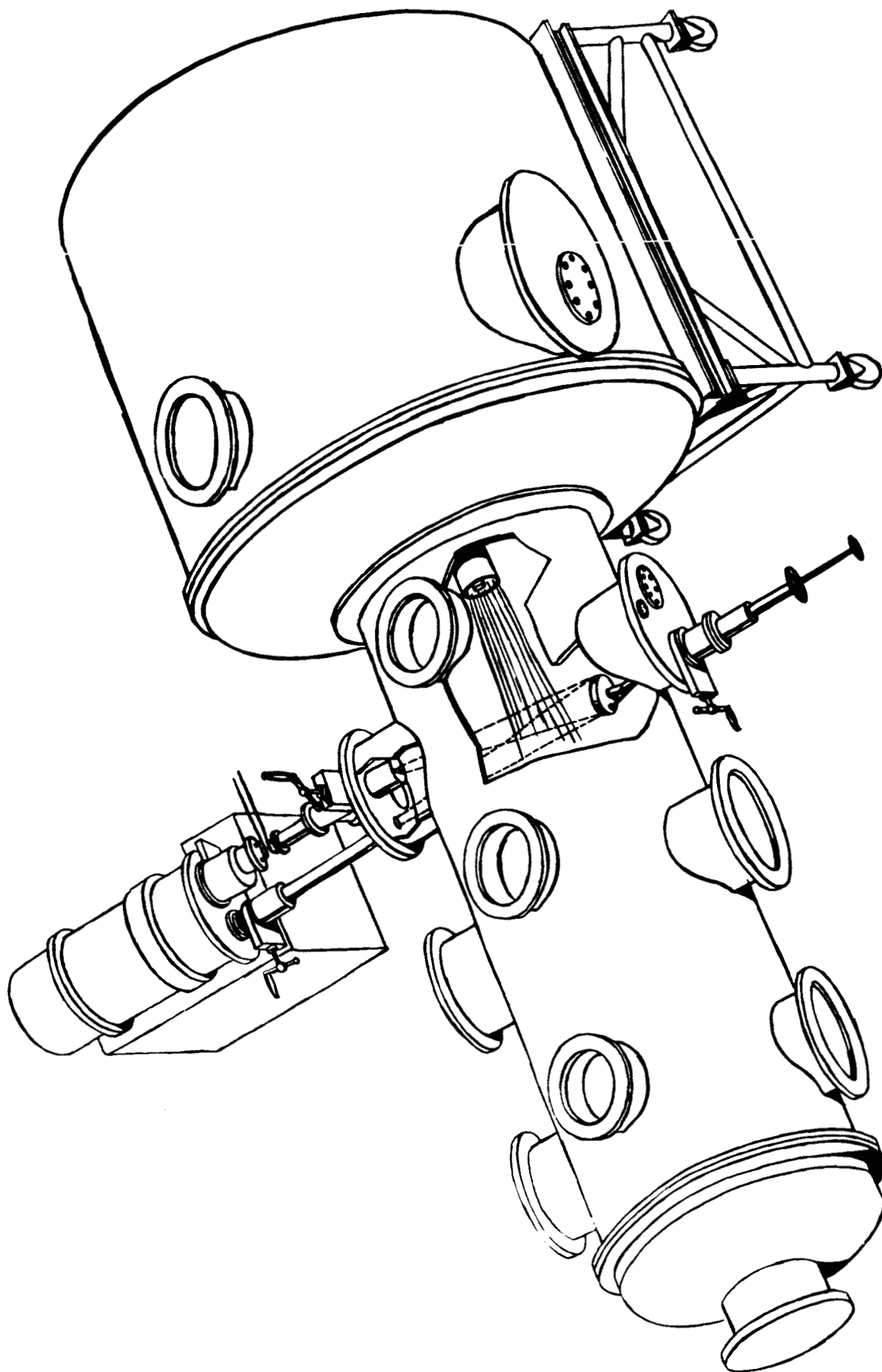
Fig. 15. Optical Arrangement for Vacuum Ultraviolet Measurements of Plasma Species

modifications of the test chamber port covers. The JACO 1-meter normal incidence vacuum ultraviolet spectrometer to be used for this purpose has been operational for some time.

5.4 Plasma Species Velocities

Direct velocity measurements are quoted here, based on luminous species time-of-flight observations. Two important factors enter in throwing such measurements in a disfavorable light: (1) most of the species present may be non-luminous and travelling with different velocities, and (2) the luminosity pulse shape might be a wave of re-combination and re-excitation moving in the plasma with a different velocity and having a different density profile than the particles them-selves.

After spectroscopic identification of the luminous species appearing in the exhaust stream of the engine, a strong spectral line for each of the major species was selected for time-of-flight and pulse shape measurements. The 0.5 meter JACO Ebert monochromator was used to isolate the lines, and the luminous signal was detected by an appropriate photomultiplier-preamplifier system, then displayed on an oscilloscope. For the sake of comparison, the total light time-of-flight signal also was recorded under the same operating conditions. An empirical basis for interpreting such observations was obtained from previous data gathered

with a rotating mirror camera under similar, but not identical,

conditions. In the previous experiments, a coaxial gun with a slotted

outer electrode had been used to observe luminous sheets forming at the

breech, and propagating toward, then finally beyond, the muzzle.

The times of appearance at the exit of the accelerator were used to

infer velocities of the ions within the accelerator, assuming the break-

down position to be near the interstage ports. A sample oscilloscope

trace of the photomultiplier signal is shown in Figure 16.

Total light signals were observed using the photomultiplier without

the monochromator both at the muzzle of the accelerator and approximately

10 cm. forward of it.

A pulse sampling technique was used to obtain a comparison with

these results. The repetitive nature of the engine allows the use of time-

resolved spectral studies of its luminous exhaust with gated photomultipliers.

Portions of each pulse of the repetitive signal from 0.1 sec to several

microseconds in width may be observed by the use of a gated photo-

multiplier and balanced electrometer. These portions were time-

averaged by the use of long time constants to obtain a steady value for

each point in the luminous pulse. Moving the gate through successive

time intervals throughout the duration of the light signal gives an accurate

average time profile of the emitted light. This technique is illustrated
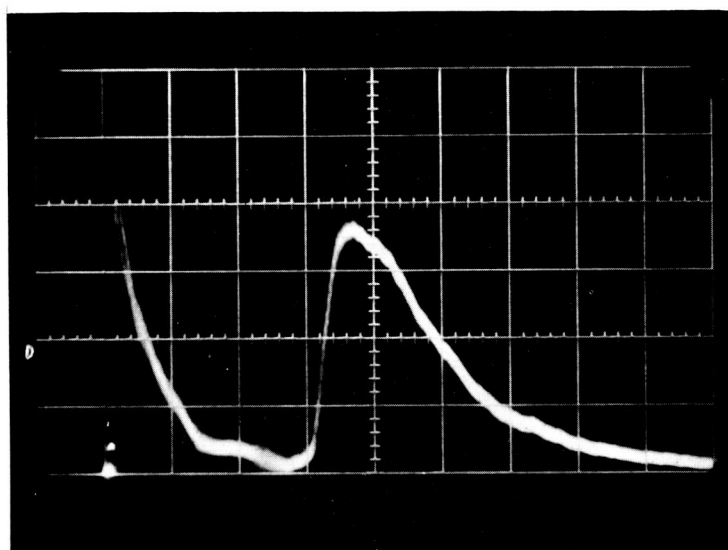
Fig. 16. Photomultiplier Signal from the He II
4685 A Line with 9 KV on the Second
Stage Storage Capacitor. Sweep 5 sec/cm.

in Figure 17. The pulsed nature of the photomultiplier supply voltage

permits higher gain operation of this detector than possible with steady

operation[7]. A higher signal-to-noise ratio results also from the

fact that photomultiplier noise is absent when the gate is closed. The

details of this technique have been published elsewhere[8].

A typical strip chart record for the 4685 A He II line is shown in

Figure 18. The average times of appearance of peak luminosity for

the He II line obtained this way were the same as those obtained by

photomultiplier observation of individual pulses. Rise time was

approximately 1.5 microseconds and pulse width 3.5 - 4 microseconds.

This pulse width is in sharp contrast with the figure 8 - 10 microseconds

obtained with the photomultiplier-preamplifier for the He II line. The

discrepancy was probably due to non-linear operation of the latter

combination, since a comparison of records for the considerably less

intense He I line indicated good agreement of the pulse shapes obtained

by the two techniques.

As an example of the drastic variation of results that can be obtained

by seemingly small variations in operating conditions, an average time

profile for the He I line obtained while the gun was mounted in a 6" pyrex

extension to the large test chamber is shown in Figure 19. The small

pulse occurring at around 6 microseconds remains inexplicable, although

the possibilities of excitation by runaway electrons or by resonant photons
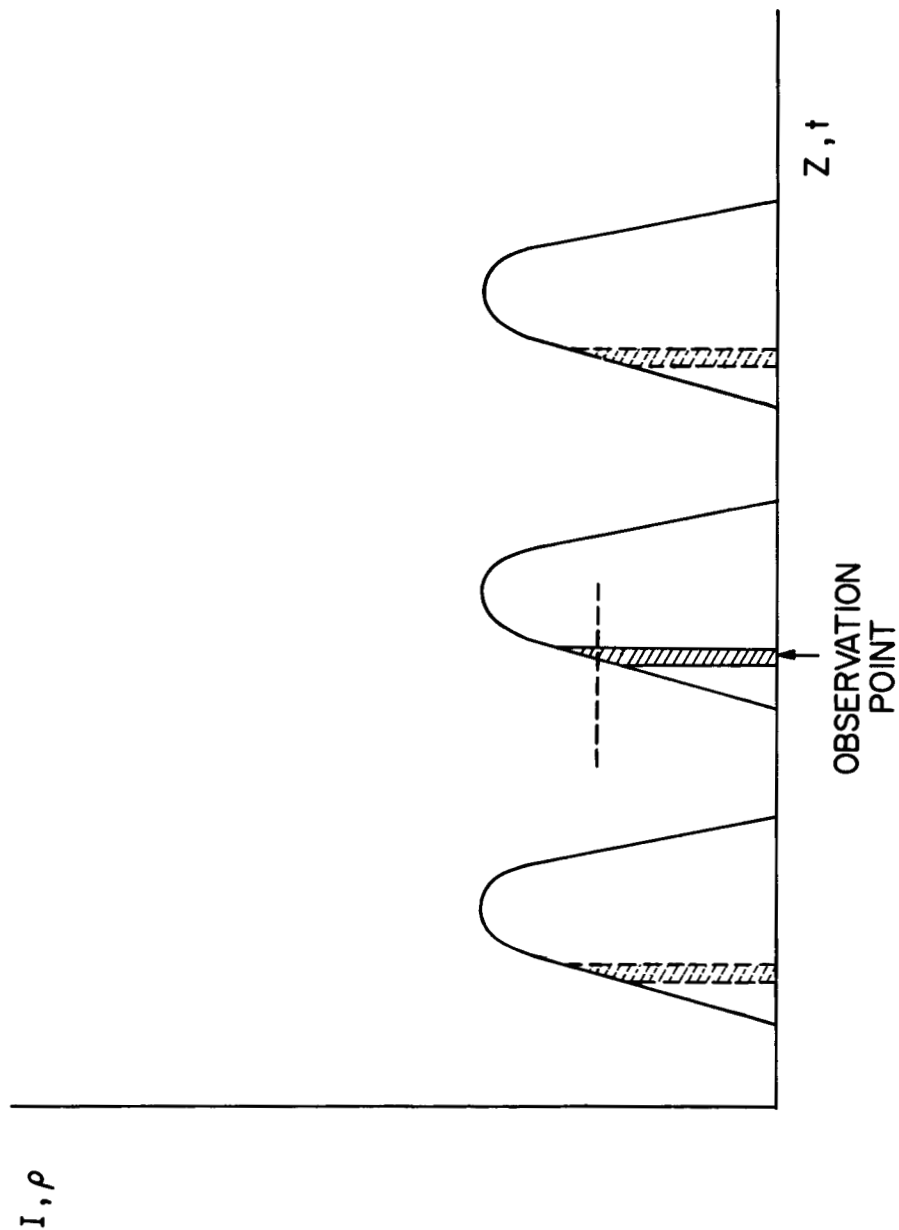
Figure 17. Schematic Description of the Pulse Sampling Technique. The shaded portions in each light signal pulse represent the portions of each pulse detected by the gated photomultiplier. Depending on the time constants chosen in the amplifier a number of these pulses are integrated and represented as an average point on the light pulse contour. The entire light pulse contour is mapped out by slowly scanning the time location of the photomultiplier gate.

-36-
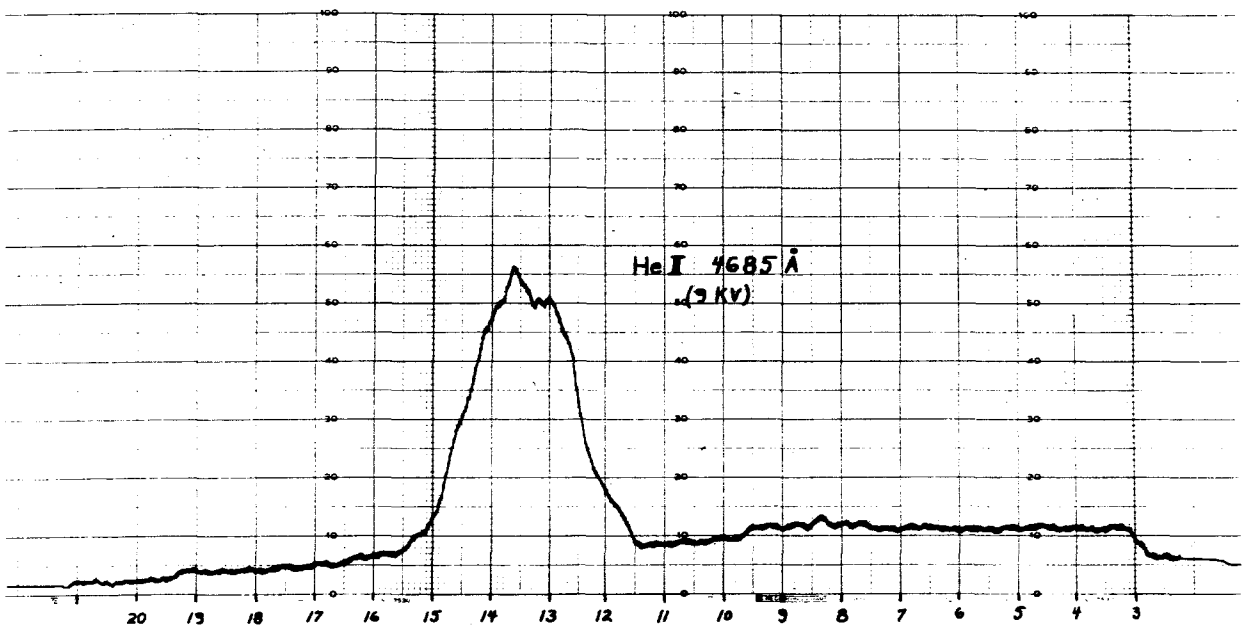
Figure 18. Strip Chart Record of the Average Pulse Shape of
the He II 4685 Å Line as Obtained by the Pulse -
Sampling Technique.

-37-
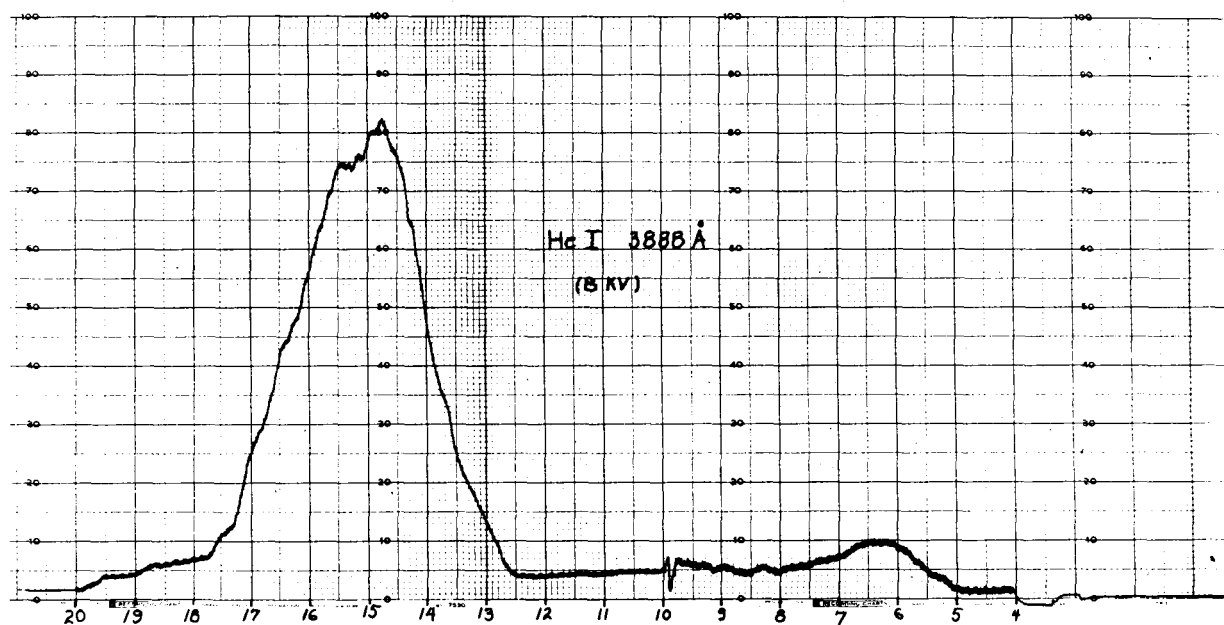
Figure 19. Strip Chart Record of the Average Pulse Shape
of the He I 3888 Å Line as Obtained by the
Pulse-Sampling Technique.

-38-

propagating in a slow-wave mode have not been eliminated. In any event, this first pulse disappears, and the second pulse becomes weaker than the He II pulse when the gun is fired directly into the large test chamber.

5.5 Input Mass Flow Rates

The gaseous mass input flow can be (and was) measured to a high degree of accuracy, per se, but has often not accurately represented the actual mass flow in the engine exhaust stream due to mass addition from electrode or insulator erosion. Also, in the particular experiments described here, part of the input mass flow was deliberately wasted for the sake of the expediency of experimental simplicity, and the fraction actually utilized was estimated only qualitatively on the basis of sonic flow in the gun barrel.

In the experiments from which the tabulated data are presented, the input mass flow was not intentionally altered, that is, the input flowmeter readings were held constant. Some qualitative observations were made as to engine performance vs input flow rates, however. The first observation to be made is that the range of flow rates is severely limited by the requirement that the discharge characteristics of the device be favorable to proper operation. They are also limited by the pumping speed of the vacuum system, as can be seen by reference to Figure 3. Within the limited range of favorable flow rates, there was a distinct improvement

in energy efficiency with a decrease in mass flow rate, all other operating conditions being held constant. The particular limited ranges of flow rates encountered changed with changes in interstage passage dimensions, shape, and location, with the background pressure in the test chamber, and with variation of obstacles near the muzzle.

5.6 Discharge Current and Voltage Transients

When carrying out experiments with a capacitor bank that has not been optimized for minimum possible inductance, it becomes especially desirable to separate external circuit losses from gun losses so that thrustor efficiency might be obtained independent of the particular energy storage and transfer system employed. At first glance, a straightforward approach to this problem would seem to be a determination of instantaneous power transfer into the gun by measuring voltage and current waveforms at the gun terminals, plotting their product on a graph, and obtaining the energy transfer by numerically integrating under the power curve. Such a procedure seems valid for the special case in which the gun circuit is over-damped and also the gun does not crowbar. In all other cases, e.g., for ringing circuits and/or crowbarring circuits, the inter-pretation of the waveforms is not straightforward.

One additional point should be made concerning the validity of using terminal measurements as a reasonable means of determining energy actually transferred into the accelerating processes. As is the case for the present experiments, it is often desirable to relax the inductance requirements in the inactive portion of the gun itself, i.e., the terminal

flanges and the cylindrical portion of the gun behind the initiating point of the current sheet, for the sake of experimental simplicity and convenience. At the same time, it can be inconvenient to obtain reliable terminal voltage measurements at the point of current sheet initiation. The result is that the measured voltage, and hence the computed energy, contains significant contributions from the inductive load in the inactive portion of the gun. This inductance, on the other hand, could be minimized in an optimum design, after the convenience of experimental flexibility is no longer required. The point, then, is that such terminal measurements, while they may yield more favorable gun efficiences than those obtainable by comparison with energy initially stored in the capacitor, will still be too conservative as a result of the location of the voltage probe. If only the energy transferred during the first half cycle of power is taken into account, the resulting thrustor efficiencies may again be too conservative at least for the conditions under which the gun emits only one sheet for one complete discharge of the capacitor. On the other hand, overly optimistic efficiences may be obtained when only the first half cycle of power is charged to the gun if several current sheets (for each half cycle of current) occur during a single complete discharge of the capacitor.

To illustrate these points, let us consider a simple L, R, C circuit as an approximation to the actual gun circuit in which L, R, C are total values of the circuit constants, L_ℓ and R_ℓ are characteristics of the gun, dL/dt is constant and included in R_ℓ dR/dt is zero, and L_ℓ includes

both the gun terminal inductance and a time-averaged coaxial line inductance of the active portion of the gun. The charge, current, and gun terminal voltage in such a circuit, with V_o as the initial voltage, are given by

$$q = CV_o \, e^{-\alpha t} \left(\frac{\alpha}{\omega} \sin \omega t + \cos \omega t \right)$$

$$i = - \frac{V_o}{\omega L} \, e^{-\alpha t} \sin \omega t$$

$$V_\ell = iR_\ell + L_\ell \frac{di}{dt} = \frac{V_o}{\omega L} \, e^{-\alpha t} \left[\left(\alpha L_\ell - R_\ell \right) \sin \omega t - \omega L_\ell \cos \omega t \right]$$

where $\alpha = \dfrac{R}{2L}$ \hfill (5.8)

$$\omega_o^2 = \frac{1}{LC}$$

$$\omega^2 = \omega_o^2 - \alpha^2$$

The instantaneous power transferred to the gun terminals is

$$P_\ell(t) = i \, V_\ell =$$

$$= \frac{V_o^2}{2\omega^2 L^2} \, e^{-2\alpha t} \left[\left(R_\ell - \alpha L_\ell \right) - \left(R_\ell - \alpha L_\ell \right) \cos 2\omega t + \omega L_\ell \sin 2\omega t \right]$$

\hfill (5.9)

and the energy at any time t is

$$E_\ell(t) = \int_0^t P_\ell(t) \, dt =$$

$$= \frac{1}{2} CV_o^2 \cdot \frac{R_\ell}{R} - \frac{1}{2} CV_o^2 \cdot \frac{\omega_o^2}{\omega^2} e^{-2\alpha t} \left[\frac{R_\ell}{R} - \frac{L_\ell}{2L} + \left(\frac{L_\ell}{2L} - \frac{\alpha^2}{\omega_o^2} \cdot \frac{R_\ell}{R} \right) \cos 2\omega t + \right.$$

$$\left. + \frac{\omega RC}{2} \cdot \frac{R_\ell}{R} \sin 2\omega t \right]$$

\hfill (5.10)

42

Equation (5.10) indicates clearly the net energy delivered to the gun

after the oscillations have damped out, i.e., as t approaches infinity:

$$E_\ell(\infty) = \frac{1}{2} CV_o^2 \cdot \frac{R_\ell}{R} \qquad (5.11)$$

The end of the first half cycle of power occurs at

$$t_1 = \frac{1}{\omega} \text{ arc tan} \left(\frac{\omega L_\ell}{\alpha L_\ell - R_\ell} \right) \qquad (5.12)$$

Equations (5.10), (5.11), and (5.12) can be used to compute the difference

$$E_\ell(\infty) - E(t_1) \gtrless 0 \qquad (5.13)$$

which is the last term in Equation (5.10) with t_1 inserted. Equation (5.13)

may be either positive or negative, depending on the values of L, R, C,

L_ℓ and R_ℓ in the circuit. If conditions are such that Equation (5.13) is

negative, an energy overshoot occurs at the end of the first half cycle

of power. (An extreme set of conditions that can lead to this is $L_\ell/L \sim 1$

and $R_\ell/R \sim 0$.) Such an overshoot is clearly the result of energy storage

in inductance of the gun terminals and the active portion of the coaxial

electrodes.

The question now arises as to what happens to the energy magnetically

stored in the gun and elsewhere in the circuit. There appear to be two

distinct modes of operation in these guns, one in which a new current

sheet forms at the breech at the end of each full cycle of power, and another

in which "crowbarring" occurs at the breech and the initial single current

loop circuit is broken into two separate current loops while current still

flows in the circuit. When crowbarring is absent, the energy stored

43

magnetically during the first half cycle of power simultaneously can recharge the capacitor and continue to drive the plasma sheet during the second half cycle of power. At the end of this cycle, the circuit current has returned to zero, the magnetic field is absent in the gun, the current sheet will have collapsed, and the complex plasma impedance will have dropped to the point where favorable conditions exist for the formation of a new current sheet at the breech capable of forward motion. Thus, the energy re-stored in the capacitor may again be usefully applied to mechanical motion, although probably not under the coupling conditions of the first sheet. When crow-barring does occur, two current loops form, both of them generated by the collapsing magnetic field stored throughout the circuit. One circulates through the moving current sheet and stationary crowbar. In this loop, the circuit is over damped since the capacitance is relatively low, and the magnetic energy is consumed in continuation of the plasma sheet motion and resistive losses. The other loop circulates through the stationary crowbar and the capacitor, usually in a ringing discharge, dissipating energy in the resistance of the external loop. (The crowbar discharge is prevented from moving forward by the pressure of the magnetic field in the gun barrel.)

Although the evidence is not conclusive, it is believed that the conditions for the experiments reported here were such that the terminal measurements gave rise to conservative estimates of the gun efficiency, since energy over-shoot was observed and multiple sheets were not.

The discharge voltage was measured across the breech flanges of the accelerator with a Tektronix high voltage probe, having an attenuation factor of 1000:1. The output of the probe with all leads was adjusted and calibrated with the signal of a previously calibrated square wave generator.

The current transients were obtained with a Ragowski loop

placed around the pyrex insulator between the second stage electrode

flanges. The integrated (R = 50 ohms, C = 1 mfd) output of the loop

was displayed simultaneously with the voltage probe signal on a dual

beam oscilloscope. A sample trace is shown in Figure 21. The loop

had been previously calibrated by obtaining a trace in which the current

had essentially damped to zero. This curve was integrated and the

resultant value, multiplied by a proportionately constant K , was

equated to the capacitor total charge. This relationship is given by

$$CV = K \int v_i \, dt$$

where v_i is the signal from the Ragowski loop integrator as seen

on the oscilloscope. C and V are capacitance and capacitor voltage

respectively. The integration was carried out both mechanically and

analytically. The analytical method assumed a current of the form

$i = I_o e^{-\alpha t} \sin \omega t_o$. I_o, α, and ω were evaluated from the

decay and ringing characteristics displayed on the traces and the

integral was evaluated between time 0 and ∞ . The mechanical

method entailed the use of a planimeter on the record of the v_i signal.

For the 45, μf case, these two methods were within 15% of each

other, the higher number being 11.2 kiloamps terminal current per

volt displayed on the oscilloscope trace. This value was used in the

subsequent discharge current measurements since it was obtained by
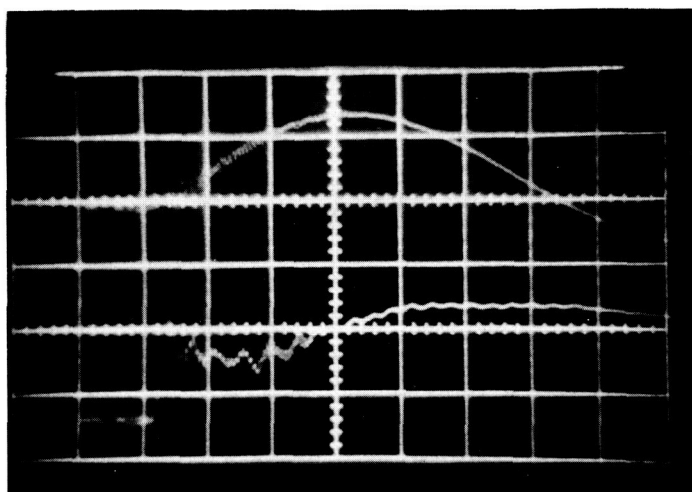
Fig. 20. Oscilloscope Trace of Voltage and Current
         Transients

Upper Current	110 K Amps/cm.
Lower Voltage	5 KV/cm.
Capacitance	45 ufd
Time Scale	1 u sec/cm.

the more accurate method of mechanical integration. Agreement on the proportionality factor K between the 45 uf case and the 15 uf case was very close, the latter being 11.0 kiloamps per volt obtained by mechanical integration.

5.7 Derived Engine Performance Parameters

A discussion of the derived quantities often given as operating parameters for pulsed plasma devices is now appropriate.

The power efficiency of pulsed plasma devices is one of the most important of the derived quantities required. There are several means of combining the measured values to obtain efficiency. Four will be discussed, but only two of the values have been deemed worth tabulating. The most conservative of these is given by

$$\eta_1 = \frac{P_c}{P_T} \quad \frac{\frac{1}{2} \dot{m} \overline{v}^2}{\frac{1}{2} \nu C V^2} \tag{5.15}$$

η_1 includes losses external to the gun, however, so the gun performance is more fairly quoted as

$$\eta_2 = \frac{P_c}{P_G} = \frac{\frac{1}{2} \dot{m} \overline{v}^2}{\nu \int_0^{t_1} i(t) V_G(t) \, dt} \tag{5.16}$$

which is still conservative, as discussed above. An optimistic value of the efficiency (as compared with η_2) is obtained from

$$\eta_3 = \frac{\frac{1}{2} T \cdot v_{luminous}}{P_T} \tag{5.17}$$

47

since the luminous pulse velocity may be higher than that of the

bulk of the gas. A high risk of misquoting true efficiency is en-

tailed also by using

$$\eta_4 = \frac{T^2}{2\dot{m}P_T} \tag{5.18}$$

since $\dot{m}$ is very difficult to measure accurately in practice, when

taking into account erosion.

The mass flow and average velocity may be derived from the

thrust balance and calorimeter readings if and only if the exact

shape of the velocity distribution is known*. With an arbitrary,

but constant shape, the following relation holds

$$v^2 = H \overline{v^2} \tag{5.19}$$

- -

*We are indebted to H. Kosmahl and P. Ramins for valuable discussions

of these points.

48

(For a Maxwellian distribution of particle velocities, $H = \frac{8}{3\pi}$).

The appropriate derived quantities then become

$$\dot{m} = \frac{T^2}{2HPc} \tag{5.20}$$

and

$$I_{sp} = \frac{2HPc}{T g} \tag{5.21}$$

The remaining error in these derived quantities is the calorimeter correction factor, which will tend to give too high an $\dot{m}$ and too low an I_{sp}. In light of this discussion, the derived quantities $\dot{m}$ and I_{sp} are tabulated as $\dot{m}H$ and I_{sp}/H, representing the direct combination of calorimeter and thrust balance readings.

6. ENGINE PERFORMANCE - DISCUSSION AND RESULTS

The engines studied during this period consisted of the following general arrangements:

Engine 1. An uncooled two-stage plasma accelerator projected into the vacuum chamber with 15 μfd capacitor and components mounted external to the chamber.

Engine 2. An oil-cooled two stage accelerator with a 15 μfd capacitor and components mounted on the thrust balance in the vacuum chamber.

Engine 3. An uncooled two-stage accelerator designed for rapid disassembly and assembly of electrodes with a 15 to 45 ufd capacitor bank

and components mounted on the thrust balance in the vacuum chamber.

6.1 Optical Measurements of Engine 1.

Engine 1 was used primarily to determine spectroscopically the luminous species present in the plasma exhaust, to measure total light and luminous species velocities and to increase the reliability of engine operation. A photograph of the electrode structure is shown in Figure 21.

Spectral records obtained by both photographic and photoelectric techniques described earlier indicated that, with respect to the visible portion of the spectrum, the plasma exhaust was remarkably free of species originating either from the copper electrodes or from the pyrex insulator. With helium as the propellant, the majority of the lines observed were those of the He II ion. In addition, some of the most intense He I lines were recorded. The relative intensity of the strong 3885 $\overset{o}{A}$ He I line was 2-3% of that of the 4685 $\overset{o}{A}$ He II line. Similar results were obtained for argon, the main difference being the apparent absence of Ar I lines. Velocities of these species obtained by the various techniques described earlier were essentially in agreement with each other and with that for the total luminosity. These velocities ranged from approximately 3 cm/microsecond with 8 KV on the second stage to about 9 cm/microsecond with 13 KV. Figure 22 shows a graph of average velocity vs. voltage. If the directed energy delivered to the plasma $(1/2\ mv^2)$ is in constant proportion to the energy per pulse delivered from the storage
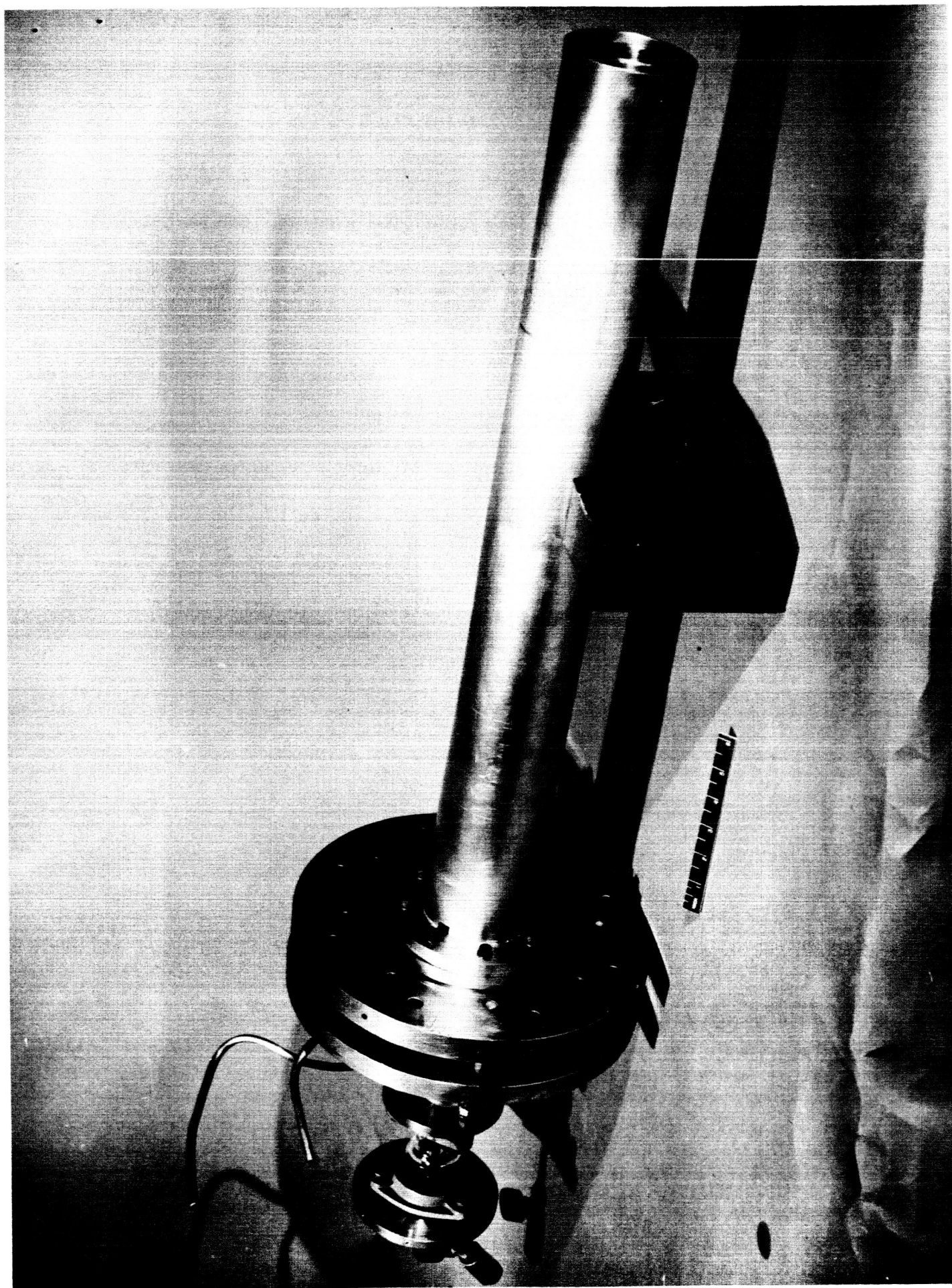
Figure 21. Electrode Structure of Engine 1.

capacitor ($1/2 \ CV^2$), if the breakdown point remains at the interstage

ports over the voltage range covered, if the mass involved remains

constant over the voltage range studied, and if the bulk of the plasma

travels at the same velocity as that of the luminous portion, then the

points in Figure 22 should lie on a straight line with a slope $(\eta \ C/m)^{1/2}$,

where η is the energy efficiency of the system. These qualifications

prevent the sensible interpretation of these results in terms of engine

performance in the absence of additional supporting data.

Total light signals were observed both at the muzzle of the accelerator

and approximately 10 cm forward of it. Velocities internal to the gun

deduced from these observations are shown also in Figure 22. They

correspond within experimental error to those obtained for the helium

ion line. Outside the gun, the inferred velocities were approximately 50%

lower than the corresponding inferred velocities inside the gun. The total

light pulses were generally slower rising and slower decaying than the

helium ion line pulses. Both the slight curvature of the array of velocity

data points and the discrepancies between interstage ports-to-muzzle and

external times-of-flight may be given reasonable interpretations at a later

time when similar data from absorption studies of non-luminous species

become available.

6.2 Operational Improvements of Engine 1

The work involved in increasing the operating reliability of the

repetitively pulsed engine was undertaken at a relatively early stage

in the contract period primarily for the purpose of providing a device

52
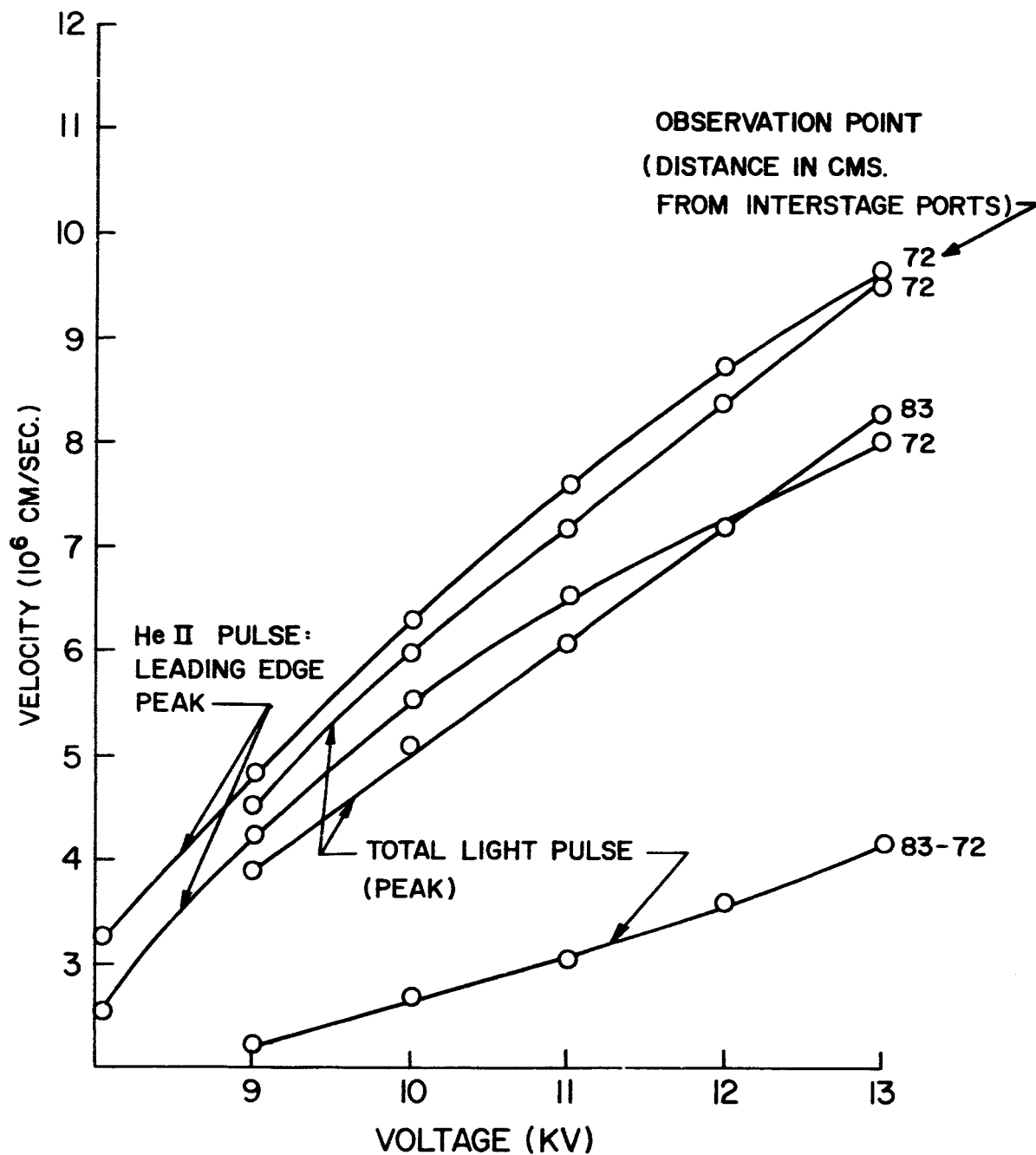
Figure 22. Graph of Luminous Front Velocity vs Voltage Data Obtained
from Oscilloscope Traces of Photomultiplier Signals

53

which could be studied with those techniques requiring repetitive pulsing for extended periods i.e., spectral pulse sampling, thrust measurement, and calorimetry. An important by-product was the discovery and partial solution of some of the problems which would be faced in future developmental programs.

The engine was fired at various pulsing rates up to 40 cps at voltages up to 13 KV using a 15 μfd capacitor. Maximum power input to the capacitor, therefore, was as high as 50 KW for durations of 3-5 minutes. The most significant problem associated with operation at levels in excess of 3 KW appeared to be that of electrode heating. This effect manifested itself in three ways:

1. Alteration of propellant density in the first stage and subsequent erratic behavior of the accelerator.

2. Structural failure of the electrodes.

3. Increased resistance of the electrodes.

The first of these problems was virtually eliminated by optimizing the slot size of the interstage ports to provide maximum propellant density in the first stage. (The slots were decreased in width from .03" to .01".) The second problem was minimized by using one piece, rather than 2 piece, construction of the central electrode. This eliminated failure due to the softening of silver soldered joints which were nearest the point of discharge breakdown. In extended runs, however, at levels in excess of 10 KW, the 1/8" wall one-piece central electrodes showed some signs of deformation.

The problem of increased electrode resistance is significant in that it was observed that, after 10 minutes of firing at 7.5 KW, electrode temperatures were of the order of 750° - 850°C. It is estimated that a rise in temperature of this order brings about a five-fold increase in the resistance of the copper electrodes. The i^2R loss to the electrode at room temperature is estimated from the peak currents and skin depth resistance (at a frequency of 10^5 sec^{-1}) to be about 5% of the total power. Thus, as much as 25% of the total power might be lost by this process at the elevated temperature. The use of electrode cooling was clearly indicated from the above considerations.

6.3 Design and Operation of Engine 2

Oil-cooling of only the breech end of the central electrode of Engine 1 failed to achieve sufficient cooling. Therefore, a two-stage accelerator with completely fluid-cooled electrodes in the second stage was designed, as shown in Figures 23-25. The design of each second stage electrode consists essentially of two concentric copper cylinders with helically-wound copper tubing sandwiched between the walls. (The inner electrode of the first stage is not directly cooled.) Diffusion pump oil is pumped down the electrode through the copper tubing and is returned through the passage formed by the electrode walls and the outside surface of the copper tubing. The electrode flanges are cooled by the same oil circulating in grooves in the flange faces. The heat sink for the hot oil is a chiled water heat exchanger. The entire cooling system was designed to handle up to 10 KW losses in the cooled capacitors and electrodes, with
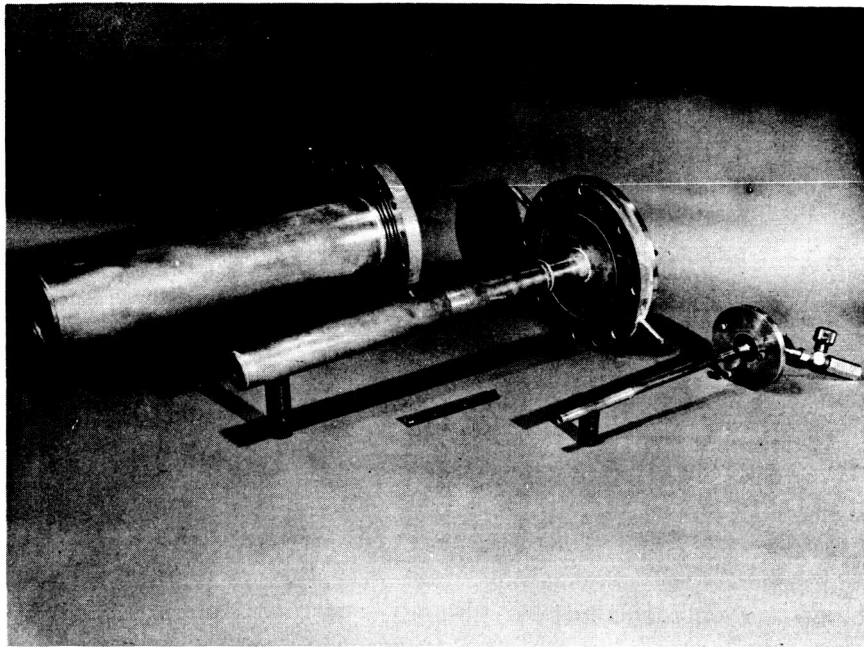
Figure 23. Electrodes of Oil Cooled Accelerator - Engine 2
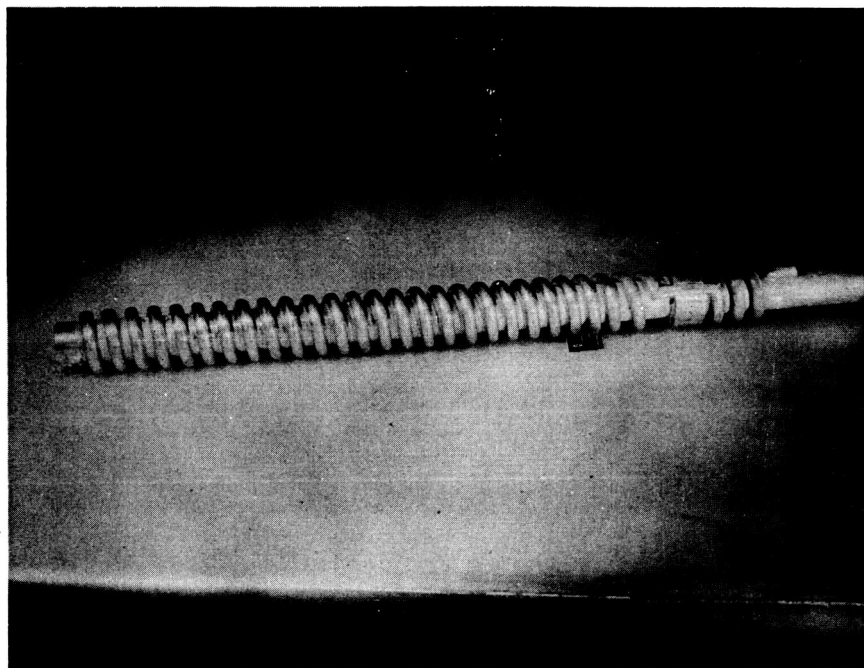
Figure 24. Interior of Electrode for Oil Cooled
Accelerator
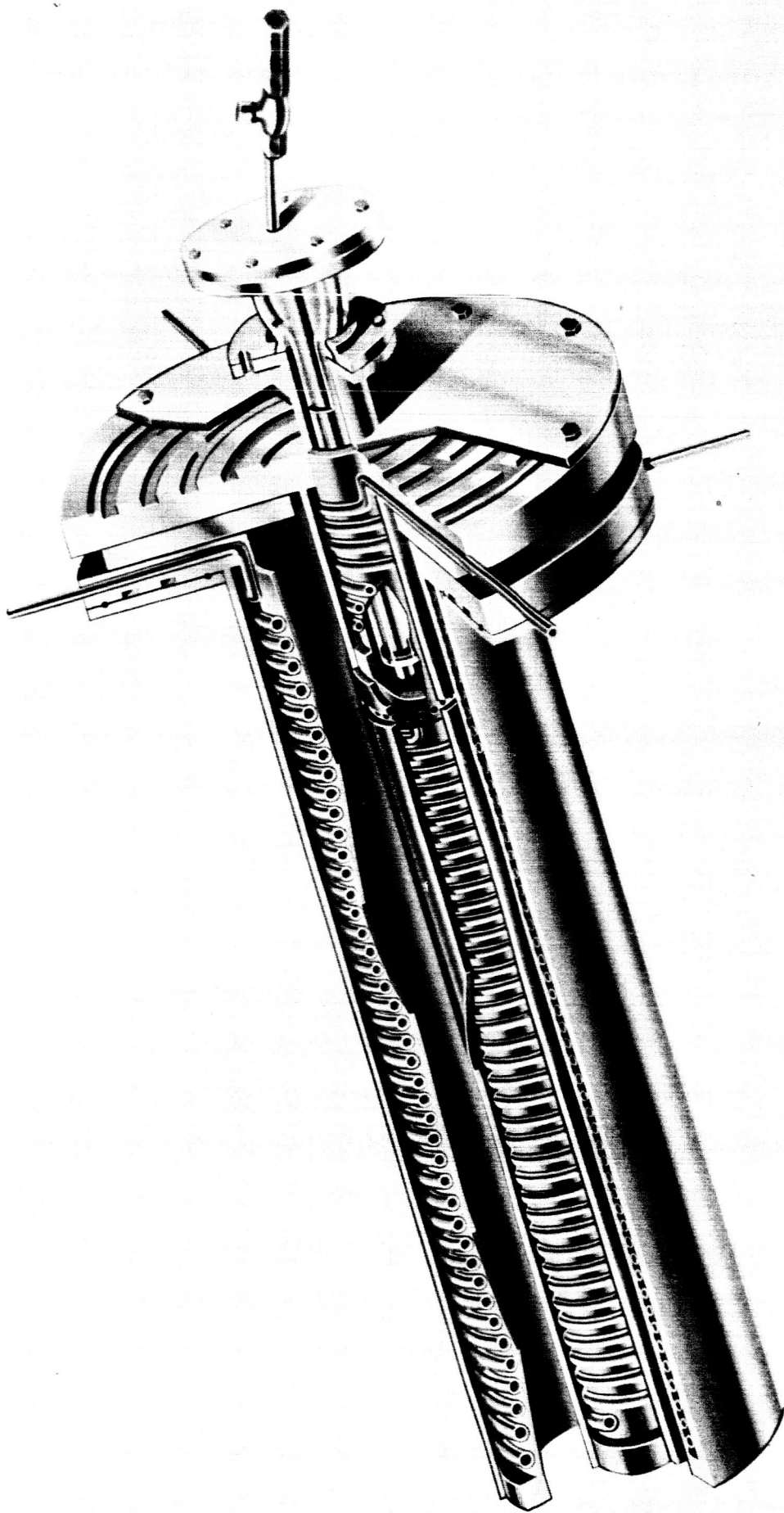
Fig. 25. Oil Cooled Accelerator Assembly

the electrodes maintained at less than 150°C at this rate of dissipation. The capacitors initially used were cooled by running cold oil from the system through double wall stamped channel plates mounted on the broad faces of the capacitor cases. The parallel plate capacitor leads were also cooled.

The engine package, consisting of first and second stage capacitors, accelerator, first-stage ignitron, and coolant, electrical and fuel lines, was mounted on the thrust balance in the addendum chamber described previously. The addendum chamber was evacuated to 10^{-6} mm Hg. The engine was test fired for runs up to 50 KW for periods up to 5 minutes with no apparent overheating (above the design point) of the electrodes. The chief difficulties encountered during operation of the engine in a vacuum were those associated with capacitor failures.

After relatively short-term operation, insulating oil leaks developed in the seals between the central low-profile insulator bushing, the capacitor case, and the high-voltage stud. In other runs where the seals did not fail, pressures which developed within the capacitor against the external vacuum caused the cases to bulge severely. The epoxy central bushing supplied with some of the capacitors also was a major source of difficulty as a result of outgassing and surface discharge across the carbon-deposited convolutions. In an effort to eliminate all of the above problems, a stainless steel capacitor housing with a glass central insulator was devised and pressed into service. This arrangement extended the life of the capacitor so that no further failures resulted with jacketed units.

The thrust level obtained with this accelerator and the 15 μfd capacitor described was generally under 9 millinewtons with 4 KW input to the capacitors. In the interest of obtaining greater flexibility of the engine for purposes of modification of insulators and electrode geometries, a set of uncooled removable electrodes was substituted and all subsequent performance measurements were made using these.

6.4 Parametric Studies of Engine 3

The accelerator used in these tests was similar in design to that of Engine 1. The capacitors used were rated at 20 KV, 15 μfd--with up to 3 capacitors assembled in parallel on the thrust balance to form a bank of 45 μfd. Engine 3 was fired up to 10 cps at 12 KV for a power input as high as 30 KW. Most measurements described here were carried out, however, at firing rates from 2-5 cps at power inputs from 5-12 KW.

The propellants studied included argon, helium and nitrogen. Under many operating conditions where argon was used; however, premature triggering of the accelerator, spurious discharge to the test chamber walls and eratic behavior, in general, took place. Helium and nitrogen minimized these effects, but the limited chamber pressure range with which helium could be used left nitrogen as the best choice of the three propellants for the particular measurements of immediate interest.

59

6.4.1 Current and Voltage Transient Measurements

The voltage and current measurements described previously were carried out on the above engine over the range of voltage from 4-12 KV and capacitance from 15-45 μfd. The resulting values of energy transfer from the capacitors to the terms of the accelerator are partially summarized in Table 1. The energy transfer efficiency was rendered less favorable than optimum by the utilization of capacitors available at the time of assembly and measures taken to provide reliable operation in vacuum on the thrust balance, i.e., terminal extensions, modified insulator spacing, and increased parallel sheet spacing all contributed toward increased external inductance. The increase in transfer efficiency with increasing capacitance is partly associated with the decreased inductance of the bank of parallel units. A greater decrease in inductance, more in proportion to the number of units, was prevented by the additional lead lengths required for connecting the capacitors to the accelerator in such a way as to permit installation on the thrust balance.

An inventory of the distributed inductances in the engine is as follows:

TABLE 1. PERFORMANCE OF THE TWO-STAGE COAXIAL ENGINE

C ufd	V_c KV	$\frac{1}{2} C V_c^2$ Joules	P in Watts	T Newtons	$E_{terminals}$ Joules	$P_{terminals}$ Watts	$P_{calorimeter}$ Watts	η_{gun} $\frac{P_{cal.}}{P_{terminals}}$	I_{sp}/H sec.	$\dot{m}H$ K_g/sec.
15	9.0	607	6070	.0048	101	1010	120	11.8%	4900	0.96×10^{-7}
45	7.2	1160	2320	.0041	400	800	208	26.0%	10,000	0.40×10^{-7}
45	9.0	1820	3640	.0085	641	1282	330	25.8%	7860	1.09×10^{-7}
45	10.0	2250	4500	.0182	791	1582	450	28.4%	4990	3.80×10^{-7}
45	12.0	3240	6480	.0342	1140	2280	988	43.5%	5830	6.00×10^{-7}

$$\nu = 2 \text{ sec}^{-1}$$

$$\dot{m}_{in} = 7.5 \times 10^{-7} K_g/sec$$

$$m_{eff.} = 0.024 \times 10^{-7} K_g/sec$$

$$H = \frac{\overline{v^2}}{\overline{v}^2} = \frac{8}{3\pi} \text{ for Maxwellian distributions}$$

Propellant - Nitrogen

Distributed Inductances in the Two-Stage Coaxial Engine

Circuit inductance up to interstage ports (estimated   .089 uh
from current ringdown)

Coaxial electrode inductance from the input flanges
to the interstage ports   .009 uh

Nominal inductance of three 15 μfd capacitors in
parallel   .017 uh

Estimated inductance of leads, including effects of
modifications to capacitor bank   .063 uh

Coaxial electrode inductance from interstage ports
to exhaust end of engine.   .053 uh

The relatively high inductance of the capacitors, the leads,

and the portion of the accelerator behind the initial discharge and

efficiency, in that a portion of the energy magnetically stored in the

external inductance is transferred back to the capacitor (with circuit

losses). It is not always possible to utilize this re-stored energy for

further acceleration. In some geometries, the re-stored energy in

the capacitor is subsequently dissipated, largely in a purely resistive

crowbar occurring at the gun breech. The insulator arrangement used

here is believed to enhance the formation of such a crowbar. In other

geometries, multiple current sheets, one for each half-cycle, have also been observed[1].

The equivalent series resistance of the capacitors (about .003 ohm for three capactors in parallel) was another important dissipative factor, since it was of the same order as the equivalent resistance due to the current sheet motion (about .005 ohm).

6.4.2 Calorimeter Measurements

Estimates of plasma kinetic energy were made using the calorimetric techniques described earlier. In order to determine accelerator efficiency, the energy delivered to the calorimeter was compared with the energy delivered to the accelerator terminals from the capacitor bank. It should be noted that the ratio of energy available at the terminals to stored energy was nearly constant over the range of voltages studied for a fixed bank capacitance. It is concluded, therefore, that the 65% increase in accelerator efficiency between 7.2 and 12 KV is associated with phenomena in the plasma of the accelerator itself. These phenomena will be examined in some detail in the analysis to be presented later.

The influence of capacitance on accelerator efficiency is demonstrated partially in Table 1. In this case, there was both an approximate two-fold increase in energy transfer efficiency when the capacitance was increased from 15 to 45 ufd, and a similar increase in accelerator efficiency. These observations will be interpreted in a later section.

6.4.3 Thrust Measurement

Results of the thrust measurements are summarized also in Table 1. For power inputs to the capacitor ranging from 2300-6500 watts, thrust levels ranged from 4 to 34 millinewtons, respectively. The thrust readings were reproducible to within 5%. For the 45 μfd bank capacitance, the thrust level of the engine was approximately proportional to the firing rate of the engine in the range 2 to 5 cps. The correlation of thrust to firing rate was not attempted with higher firing rates since the time constant of the charging network used in these runs was too long to maintain the set power supply voltage and, hence the power input to the energy storage capacitors was not conveniently determined.

6.4.4 Specific Impulse

Some measurements of plasma velocity were made using the total light photoelectric techniques described earlier. These measurements appear to indicate a lack of dependence of luminous front velocities on capacitor bank size, in the range of 15 to 45 microfarads, all other conditions being equal. Velocities from 3 cm/usec to 7.5 cm/usec were obtained for capacitor voltages from 6-12 KV with N_2 as the propellant. Since these velocities are those possibly of only a portion of the exhaust stream, an accurate estimate of engine specific impulse from $I_{sp} = \dfrac{V}{g}$ cannot be made.

The calorimeter power and thrust measurements were used to tabulate (Table 1) a value related to I_{sp} through the velocity distribution form factor, H, as discussed previously.

63

Since H cannot be assumed Maxwellian, and, in fact, is not generally known for these experiments, $2 P_c / T_g = I_{sp} / H$ is presented to provide an indication of the trend in I_{sp} only. It should be noted that the observed trend is in disagreement with the trend observed in the measurements of luminous front velocities. A possible source of this disagreement is mass addition from the electrodes and insulator either by erosion or desorption, which would affect the amount thrust delivered by the engine but would not necessarily affect the velocity of the current sheet.

6.4.5 Mass Utilization

The measured flow of nitrogen propellant through the engine for all the data tabulated was 7.5×10^{-7} kg./sec. Since the time to fill the barrel of the accelerator (sonically) was approximately 1.6 milli-seconds, the amount of gas actually available at a firing rate of 2 cps was about 2.4×10^{-9} kg./sec.

The calculation of the effective mass flow for the engine, $\dot{m}$, depends also on the velocity distribution form factor H. We have there-fore presented the calculated values of $T^2/2 P_c$ as values for $\dot{m}$ H. The approximate fifteen-fold increase in the values of $\dot{m}$ H with increasing voltage indicates, assuming only small changes in H, the presence of mass addition. The values of $\dot{m}$ H are 16 to 240 times the effective mass flow of nitrogen available in the volume of the 2nd stage of the

64

accelerator. Taking into account the volume and pressure of the

first stage of the engine, complete injection of gas from the first

stage into the second would only double the effective mass flow as

computed above. One source of mass in addition to the effective

mass flow may be the surface layer of gas adsorbed on the electrode

and insulator walls between pulses. This contribution cannot be

discounted without further proof since the mass ($\sim 10^{-7}$ Kg) and the

time for adsorption ($\sim 10^{-7}$ sec /p(mm) of a monolayer of gas on the

internal surfaces are both of the proper order of magnitude to account

for the entire amount of added propellant. A more obvious possible

source of additional mass is the erosion of the insulator and electrodes.

Since spectral data on the exhaust stream of Engine 3 are not available,

it is impossible at this point to distinguish between these two possibilities

for Engine 3. Engine 1 data, however, would seem to favor the former

possibility.

7. ANALYSIS OF THE RESULTS

The results obtained in this program are examined in the light of a simplified anisotropic shock model for the coaxial gun, from which trends in the gun operating characteristics may be predicted, to a limited extent.

7.1 The Conservation Equations [*]

The equations expressing of mass, momentum and energy across a discontinuous surface moving in the coaxial gun may be written as [9]

$$\rho_1 \overline{v}_1' = \rho_2 \overline{v}_2' \tag{7.1}$$

$$P_1 + \rho_1 v_{1n}'^2 + (B_{1t}^2 - B_{1n}^2)/2\mu_0 = P_2 + \rho_2 v_{2n}'^2 + (B_{2t}^2 - B_{2n}^2)/2\mu_0 \tag{7.2}$$

$$\rho_1 v_{1n}' (\frac{1}{2} v_1'^2 + w_1) + v_{1n}' \frac{B_1^2}{\mu_0} - \frac{B_{1n} \overline{v}_1' \cdot \overline{B}_1}{\mu_0} =$$

$$= \rho_2 v_{2n}' (\frac{1}{2} v_2'^2 + w_2) + v_{2n}' \frac{B_2^2}{\mu_0} - \frac{B_{2n} \overline{v}_2' \cdot \overline{B}_2}{\mu_0} \tag{7.3}$$

$$\rho_1 v_{1n} \overline{v}_{1t} - B_{1n} \overline{B}_{1t}/\mu_0 = \rho_2 v_{2n} \overline{v}_{2t} - B_{2n} \overline{B}_{2t}/\mu_0 \tag{7.4}$$

----

[*] The authors wish to acknowledge helpful discussions with F. W. Mezger on the topics in this section.

where the subscripts t and n denote vector components tangential

and normal, respectively, to the discontinuous, moving surface, w

denotes enthalpy, quantities with bars are vectors, and the primes

denote shock coordinates.

Several assumptions, based on various qualitative experimental

observations[1, 2, 3, 4, 10], will be used to simplify Equations (7.1) to

(7.4). First of all, it will be assumed that the current sheet may be

enclosed (for the duration of its traversal of the coaxial gun) between

two imaginary surfaces of constant separation normal to the gun axis

and moving with the velocity of the leading edge of the current sheet.

(See Figure 26). These two surfaces must be separated sufficiently

to permit excursions from a flat disc shape on the part of the current

sheet, but it is assumed that such excursions are sufficiently small

so that collisions between accelerated particles may be neglected in a

time $\Delta t = \Delta x/v_s$ (see Figure 1), where Δx and v_s denote, respectively,

the distance between, and the velocity of, the two imaginary surfaces.

It is assumed also that no further accelerating processes occur outside

these moving boundaries. Equations (7.1) to (7.4) then may be applied

by assigning the subscript 1 to the region ahead of the leading surface

and the subscript 2 to the region behind the trailing surface.

The next assumption is that the shock is collisionless, i.e. the

temperature behind the shock is essentially the same as that ahead.

67
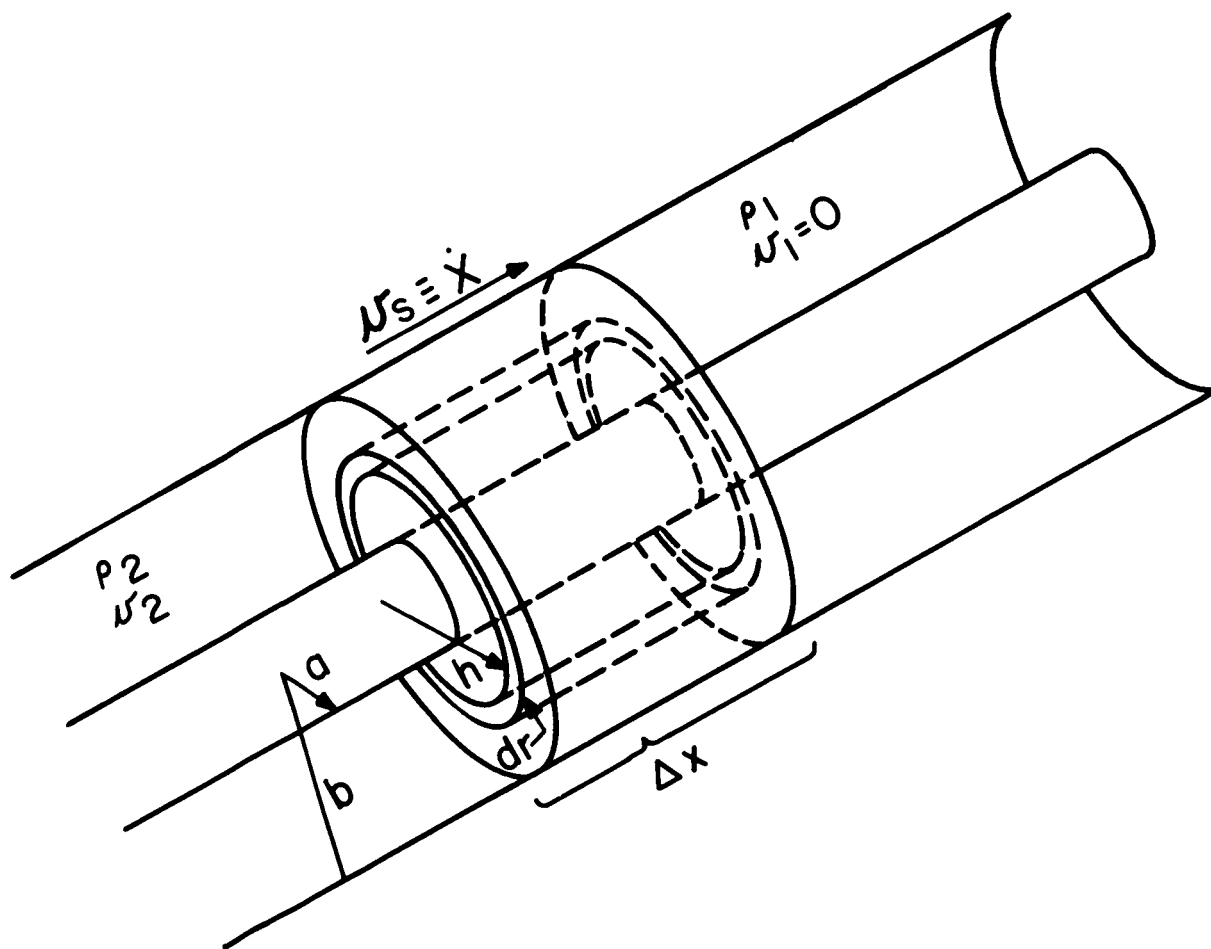
Figure 26.   Sketch of the Imaginary Current Sheet Enclosure

This is based on the observation[1,2,3,4] that there is little apparent

lateral spreading of the plasma as it leaves the muzzle of the gun. While

spreading may imply a temperature change across the sheet, a small

amount of spreading will still permit the assumption that $w_2 << \frac{1}{2} v_2'^2$.

It is also assumed that the pressures p_1 and p_2 may be neglected

in comparison with $B_2^2 /2\mu_o$ so that they may be dropped in

Equation (7.2). This is justified as long as the gun current is over

10^4 amperes, at which value the magnetic pressure, $B_2^2 /2\mu_o$ is

the order of 1 mm, and/or the gas pressure in the gun is below 1 mm.

Peak currents under the experimental conditions of the present work

were in the $10^5 - 10^6$ amperes range and gun pressures generally were

below 1 mm, so this assumption is valid over most of the path of the

current sheet in the gun, the exception being the immediate vicinity of

the initial and terminal points of the sheet motion. Both of these

assumptions are applied in dropping w_1 and w_2 from Equation (7.3).

Since it is an experimental fact[10] that only an azimuthal magnetic

field exists behind the current sheet, the following conditions may be

stated:

$$B_1 = B_{1n} = B_{2n} = B_{1t} = 0 \tag{7.5}$$

$$B_2 = B_{2t} = B_\theta \tag{7.6}$$

Using the conditions of Equations (7.5) and (7.6) and the preceding

assumptions, Equations (7.1) to (7.4) can be rewritten as

$$\rho_1 \overline{v_1'} = \rho_2 \overline{v_2'} \tag{7.7}$$

69

$$\rho_1 v_{1n}'^2 = \rho_2 v_{2n}'^2 + B_\theta^2 / 2\mu_o \tag{7.8}$$

$$\frac{1}{2}\rho_1 v_{1n}'^3 = \frac{1}{2}\rho_2 v_{2n}'^3 + \frac{B_\theta^2}{\mu_o} v_{2n}' \tag{7.9}$$

$$\rho_1 v_{1n} \overline{v}_{1t} = \rho_2 v_{2n} \overline{v}_{2t} \tag{7.10}$$

Now, $\overline{v}_{1t} = 0$, so Equation (7.10) needs be considered no longer, except that it permits writing Equation (7.7) in the scalar form

$$\rho_1 v_{1n}' = \rho_2 v_{2n}' \tag{7.11}$$

Finally, Equations (7.8) to (7.11) will be transformed (non-relativistically) into laboratory coordinates by

$$\begin{aligned} v_{1n}' &= v_s \\ v_{1n}' &= v_s - v_2 \end{aligned} \tag{7.12}$$

where v_s is the velocity of the current sheet and v_2 is the flow velocity behind the current sheet. The result is

$$\rho_1 v_s = \rho_2 (v_s - v_2) \tag{7.13}$$

$$\rho_1 v_s^2 = \rho_2 (v_s - v_2)^2 + B_\theta^2 / 2\mu_o \tag{7.14}$$

$$\frac{1}{2}\rho_1 v_s^3 = \frac{1}{2}\rho_2 (v_s - v_2)^3 + \frac{B_\theta^2}{\mu_o}(v_s - v_2) \tag{7.15}$$

Equations (7.13) and (7.14) may be solved simultaneously to give

$$v_2 = \alpha v_s \tag{7.16}$$

$$\rho_2 = \frac{\rho_1}{1 - \alpha} \tag{7.17}$$

70

where $\alpha = B_\theta^2 / 2\mu_o \rho_1 v_s^2$ $\qquad$ (7.18)

Multiplying Equation (7.15) by the factor $1/2\, \rho_1 v_s^2 (v_s - v_2)$

and substituting Equations (7.16), (7.17), and (7.18) in the result,

an expression is found for α:

$$\frac{1}{4(1 - \alpha)} = \frac{1 - \alpha}{4} + \alpha \qquad (7.19)$$

for which the solutions are

$$\alpha = 0,\ 2/3$$
$\qquad$ (7.20)

of which only the second is physically acceptable for $B_\theta \neq 0$.

It is evident that α is independent of the radial position, r.

If v_s is assumed independent of r, Equations (7.20) and (7.18) are in-

consistent with each other, since

$$B_\theta = \frac{\mu_o I}{2\pi r} \qquad (7.21)$$

This implies that Equations (7.1) to (7.4) may not properly be applied

to a situation where any of the quantities have a radial dependence, and

that, strictly speaking, modified equations should be applied, possibly

in an integral form, to permit local, but not overall, violations of the

conservation laws. For the sake of simplicity at this point, therefore,

the additional assumption is made that the use of an _averaged_ magnetic

pressure in place of $B_\theta^2 / 2\mu_o$ in all of the preceding equations will

permit a reasonable approximation to the actual conditions, i.e., that

radial flows may be neglected in comparison with axial flows. This

is the least satisfactory assumption that is made for this model, but

71

it will, at least, permit solution of the problem and prediction of

trends in the coaxial gun operating characteristics.

The average magnetic pressure across the current sheet is

given by

$$\overline{B_\theta^2}/2\mu_o = \frac{1}{2\mu_o} \frac{1}{A} \int_a^b B_\theta^2 \, 2\pi r dr$$

$$= \frac{\mu_o I^2}{4\pi A} \, \ell n \, b/a$$

or, $\quad \overline{B_\theta^2}/2\mu_o = \dfrac{L'}{2A} I^2$

where $\quad A = \pi(b^2 - a^2)$

$$L' = \frac{\mu_o}{2\pi} \, \ell n \, b/a \tag{7.22}$$

Equations (7.18), (7.20), and (7.22) may be solved simultaneously

to obtain the relationship between the coaxial gun current and the

current sheet velocity:

$$I(x,t) = 2 \left(\frac{A}{3L'}\right)^{1/2} \rho_1^{1/2}(x) \, v_s(t) \tag{7.23}$$

7.2 The Functional Form of $\rho_1(x)$

In order to completely determine the relationship between the

current sheet velocity and the gun current (Equation 7.23), it is

necessary to specify the functional form of the density ahead of the

sheet. A straightforward form that might be chosen is a power

series,

$$\rho_1(x) = \sum_{i=0}^{\infty} \rho_i' x^i \tag{7.24}$$

If $\rho_1(x)$ is a polynomial with known coefficients, Equation (7.28)

can be solved by machine methods. It is interesting to note that

various models may be covered by this representation, e. g.

$$\rho_1(x) = \rho_o' \qquad : \quad \text{slug model; current sheet model with uniform density distribution ahead of the disturbance.}$$

$$\rho_1(x) = \rho_1' x \qquad : \quad \text{snowplow-model; shock-ahead-of-current sheet model.}$$

$$\rho_1(x) = \rho_o' - \rho_1 x \qquad : \quad \text{current sheet model with linearly decreasing density distribution.}$$

For the purpose of the present discussion, the following series[*]

will be used to approximate the density distribution in the coaxial

gun barrel just prior to current sheet formation:

$$\rho_1(x) = \rho_o \, e^{-\frac{2x^2}{\ell_o^2}} \tag{7.25}$$

in which ℓ_o is some characteristic length in the gun barrel.

Equation (7.25) will closely approximate the gas distribution resulting

from pulsed gas injection since diffusion theory gives the result that

if there exists initially a delta function distribution,

$$\rho(x, o) = \frac{M}{A} \, \delta(x) \tag{7.26}$$

73

Then, after a time t, the density distribution will be described by:

$$\rho(x, t) = \frac{M}{A} \left(\frac{D}{2\pi t} \right)^{1/2} e^{-\frac{x^2 D}{t}}$$ (7.27)

Here, D is the diffusion constant and M is the total mass distributed uniformly over the area A in the initial delta function distribution. Equation (7.25), then, is equivalent to assuming the gun is fired at such a time t that $t / D \approx 1_{o}^{2}$

7.3 The Operating Characteristics of the Coaxial Gun

It is possible on the basis of this model to write expressions for the energy efficiency, the specific impulse, the average mass flow, and the thrust of the coaxial gun.

Since it is evident from Equation (7.13) that the mass flow through the trailing edge of the current sheet is $\rho_1 v_s = \rho_2(v_s - v_2)$ and since the kinetic energy per unit mass behind this edge is $v_2^2/2$ <u>in the laboratory coordinate system</u>, the mechanical power flow through the trailing edge, <u>in the laboratory coordinate system</u> is

$$P_{mech} = \frac{1}{2} \rho_1 v_s v_2^2 \cdot A$$ (7.28)

Equations (7.16), (7.17), and (7.20) may be used to rewrite Equation (7.28) as

$$P_{mech}(x, t) = \frac{2A}{9} \rho_1(x) v_s^3(t)$$ (7.29)

74

Using the identity,

$$v_s \frac{dx}{dt} \equiv \dot{x} \tag{7.30}$$

the energy delivered during the first half cycle of current can be written as:

$$E(t_2) = \frac{2A\rho_o}{9} \int_o^{x(t_2)} e^{-\frac{2x^2}{\ell_o^2}} \dot{x}^2 \, dx \tag{7.31}$$

and the efficiency of energy transfer to the plasma is:

$$\eta = \frac{4A\rho_o}{9 C_o V_o^2} \int_o^{x(t_2)} e^{-\frac{2x^2}{\ell_o^2}} \dot{x}^2 \, dx \tag{7.32}$$

It should be noted that the accelerating efficiency will be less than this since subsequent randonization of the plasma motion and wall collisions have not been taken into account.

By an argument similar to that used to obtain Equation (7.28), the total momentum flow through the trailing edge is given by

$$\tau = \rho_1 v_s v_2 A = \frac{2A}{3} \rho_1 v_s^2 \tag{7.33}$$

Since the average thrust delivered by the repetitively fired coaxial gun is the impulse per shot times the pulsing frequency, ν, the thrust may be written as:

$$T \leq \frac{2\nu A\rho_o}{3} \int_o^{x(t_2)} e^{-\frac{2x^2}{\ell_o^2}} \dot{x} \, dx \tag{7.34}$$

The inequality sign is required since again the plasma randomization and wall collisions have been neglected. It is a trivial matter to write the mass flow equation from Equation (7.13):

75

$$\dot{m} = \nu A \rho_o \int_o^{t_2} e^{-\frac{2x^2}{\ell_o^2}} \dot{x} \, dt = \nu A \rho_o \int_o^{x(t_2)} e^{-\frac{2x^2}{\ell_o^2}} dx \qquad (7.35)$$

The specific impulse is defined as

$$I_{sp} \equiv \frac{T}{\dot{m}g} \leq \frac{2}{3g} \cdot \frac{\int_o^{x(t_2)} e^{-\frac{2x^2}{\ell_o^2}} \dot{x} \, dx}{\int_o^{x(t_2)} e^{-\frac{2x^2}{\ell_o^2}} dx} \qquad (7.36)$$

For ideal gas loading in the gun, ℓ_o should be adjusted so that

$$\int_o^{x(t_2)} e^{-\frac{2x^2}{\ell_o^2}} dx \approx \frac{1}{2} \left(\frac{\pi \ell_o}{2}\right)^{1/2} \qquad (7.37)$$

7.4 The Circuit Equation

The potential drop around the closed circuit of the coaxial gun may be stated generally as

$$\frac{Q(t)}{C(t)} + R(t) I(t) + \frac{d}{dt}\left(L(t) I(t)\right) = 0 \qquad (7.38)$$

where $C(t) = Co + C' \, x(t) \approx C_o$

$$R(t) = R_o + R' \, x(t) + R_p(t) \approx R_o$$

$$L(t) = L_o + L' \, x(t)$$

The approximations listed under Equation (7.38) will be assumed part of the model for the operation of the coaxial gun, for the sake of simplicity, although it must be realized that R(t) is not necessarily even approximately constant in time, and L(t) must include the mutual inductances[11] between the differential current discs in an extended current sheet.

Using Equations (7.23) and 7.30) to eliminate the current in

Equation (7.38), and Equation (7.25) to express $\rho_1(x)$, the following

result is obtained,

$$
A_1 - B \int_0^x \left[e^{-\frac{x^2}{\ell_0^2}} + e^{-\frac{x^2}{\ell_0^2}} \right] - C \frac{dx}{dt} - \left(\frac{dx}{dt}\right)^2
$$

$$
- D \frac{d^2 x}{dt^2} - x \frac{d^2 x}{dt^2} + \frac{2D}{\ell_0^2} x \left(\frac{dx}{dt}\right)^2
$$

$$
+ \frac{2}{\ell_0^2} x^2 \left(\frac{dx}{dt}\right)^2 = 0
\tag{7.39}
$$

where

$$
A_1 = \frac{3^{1/2}}{L' A} \frac{V_o}{2\rho_o^{1/2}}
$$

$$
B = \frac{1}{L' C_o}
$$

$$
C = \frac{R_o}{L'}
$$

$$
D = \frac{L_o}{L'}
$$

No closed form solution has been found for Equation (7.39), but it may

be programmed for machine computation.

7.5 Results from the Computer Program, and Comparison with Experiment.

Equation (7.39) was programmed for solution by an analogue

computer using the following set of conditions:

$$
V_o = 10,000 \text{ volts}
$$

$$
C_o = 15, \ 24, \ 45, \text{ and } 60 \text{ microfarads}
$$

$$
R_o = 0.01 \text{ and } 0.001 \text{ ohms}
$$

77

L_o = 6.9 and 20.7 nanohenries

ℓ_o = 0.2 meter

ρ_o = 2.19 x 10^{-2}, 2.19 x 10^{-3}, 2.19 x 10^{-4},

2.19 x 10^{-5} Kg/m^3

(= 10, 1, 0.1, .01 mm of argon.)

a = 1.9 x 10^{-2} meters

b = 3.8 x 10^{-2} meters

ℓ_g ≥ 0.2 meter (This parameter, the gun length,

does not enter explicitly into the theoretical model.)

These values yield the following gun characteristics:

L' = 138 nanohenries/meter

A = 3.44 x 10^{-3} meter^2

$2\left(\dfrac{A}{3\,L'}\right)^{1/2}$ = 1.82 x 10^2 meters$^{3/2}$ hy$^{-1/2}$ (for Equation

(7.23)) and the following coefficients for Equation (7.29):

A_1 = 2.69 x 10^9, 8.49 x 10^9, 26.9 x 10^9, and 84.9 x 10^9

B = 4.81 x 10^{11}, 3.00 x 10^{11}, 1.60 x 10^{11}, and

1.20 x 10^{11}

C = 7.21 x 10^4 and 7.21 x 10^3

D = 0.05 and 0.15

The $\dot{x}$ - curves generated from these parameters are shown in

Figures 27 and 28. Using these curves, one obtains values for the

circuit current and velocity behind the current sheet by using Equations

(7.23) and (7.16).
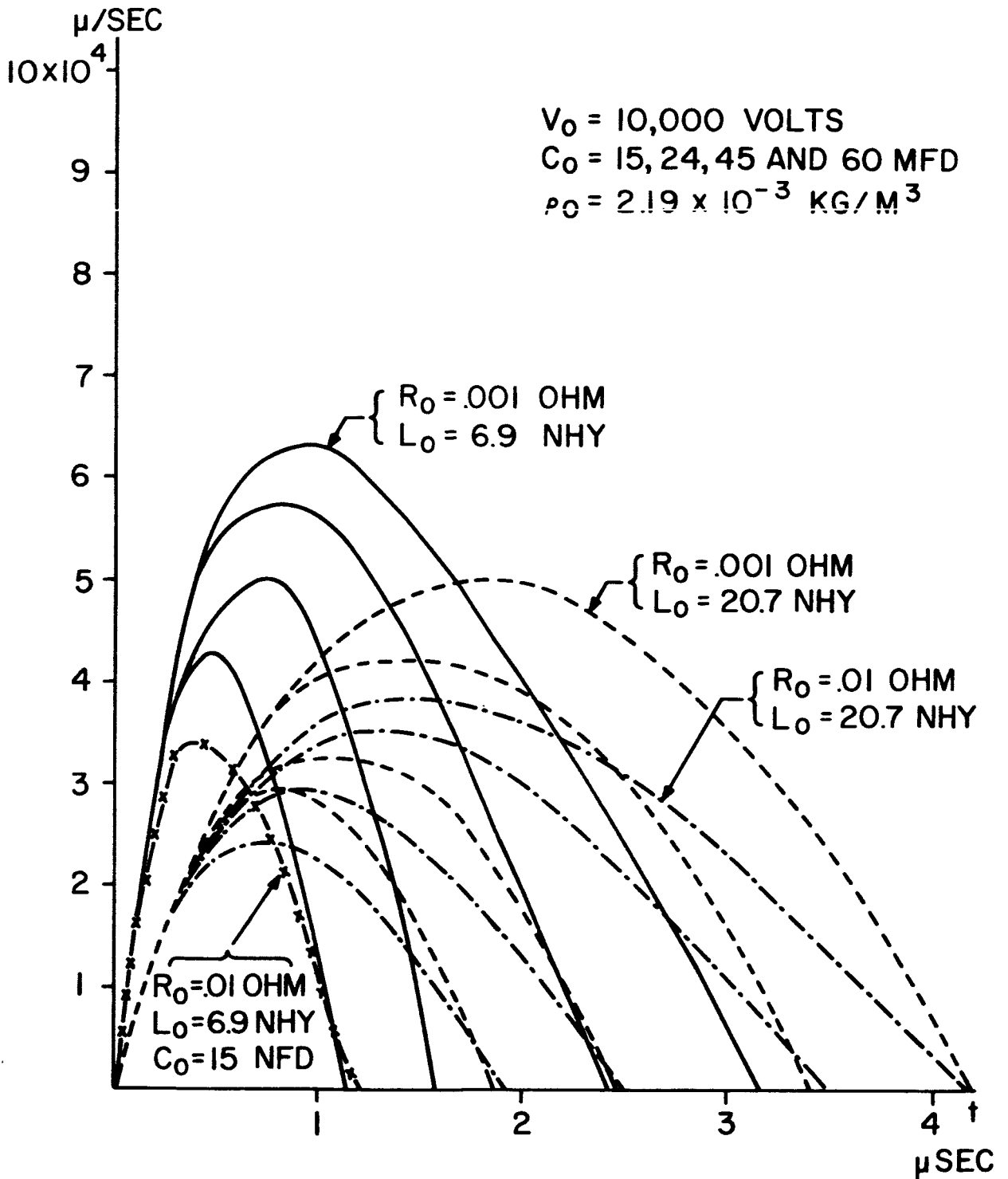
Figure 27. Variation of Current Sheet Velocity with C_0 for Various Values of R_0 and L_0
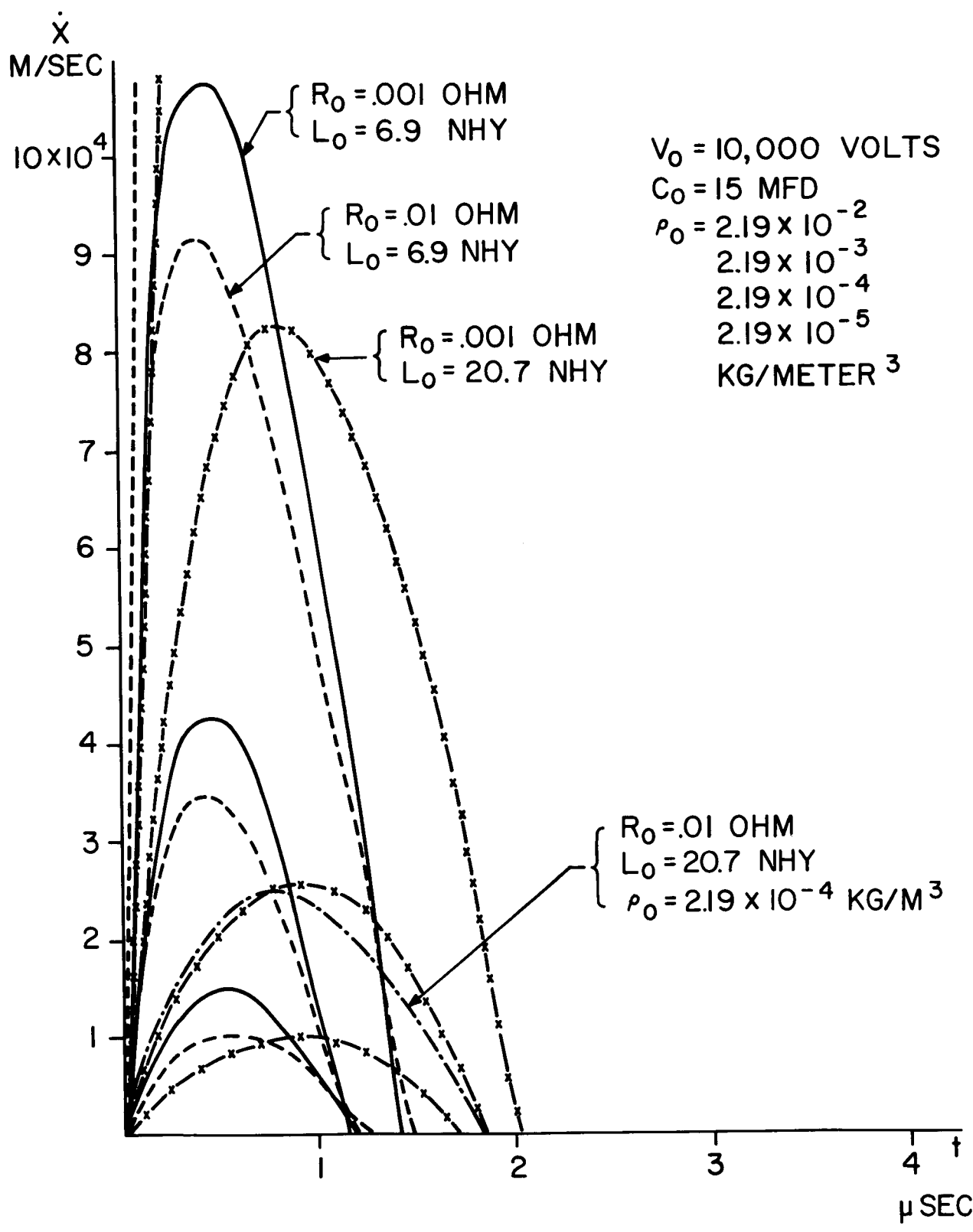
Figure 28. Variation of Current Sheet Velocity with ρ_o for Various Values of R_o and L_o

Equations (7.31) to (7.36) may be evaluated by using the parametric

relations $\dot{x} = \dot{x}(t)$ and $x = x(t)$ obtained from the computer to plot

$\dot{x} = \dot{x}(x)$ and various powers thereof to permit the required integrations

by graphical means.

The $E(t)$ curves generated from the listed parameters (by machine-

integration) are shown in Figures 29 and 30. From these curves, one

can predict a number of interesting trends, to be verified experimentally.

As expected, the efficiency of the device increases as either the

initial inductance or resistance (or both) is decreased. A factor three

decrease in L_0 increased the efficiency between 1.5 and 1.9 times

(depending on the other circuit values) whereas a factor 10 decrease in

R_0 increased the efficiency about three times, in the range of parameters

investigated. The trend with inductance has been qualitatively observed

in the experiments. The trend with resistance has not been tested.

A more subtle trend indicated by the $E(t)$ curves is the increase

of efficiency with circuit capacitance, all other conditions being fixed.

At first glance, the data in Table 1 might tend to verify this predicted

trend. The observed increases are considerably higher than predicted,

however, undoubtedly because the initial inductance was automatically

decreased with the increase in capacitance. The predicted trend is

that the efficiency increases by a factor roughly half of that by which
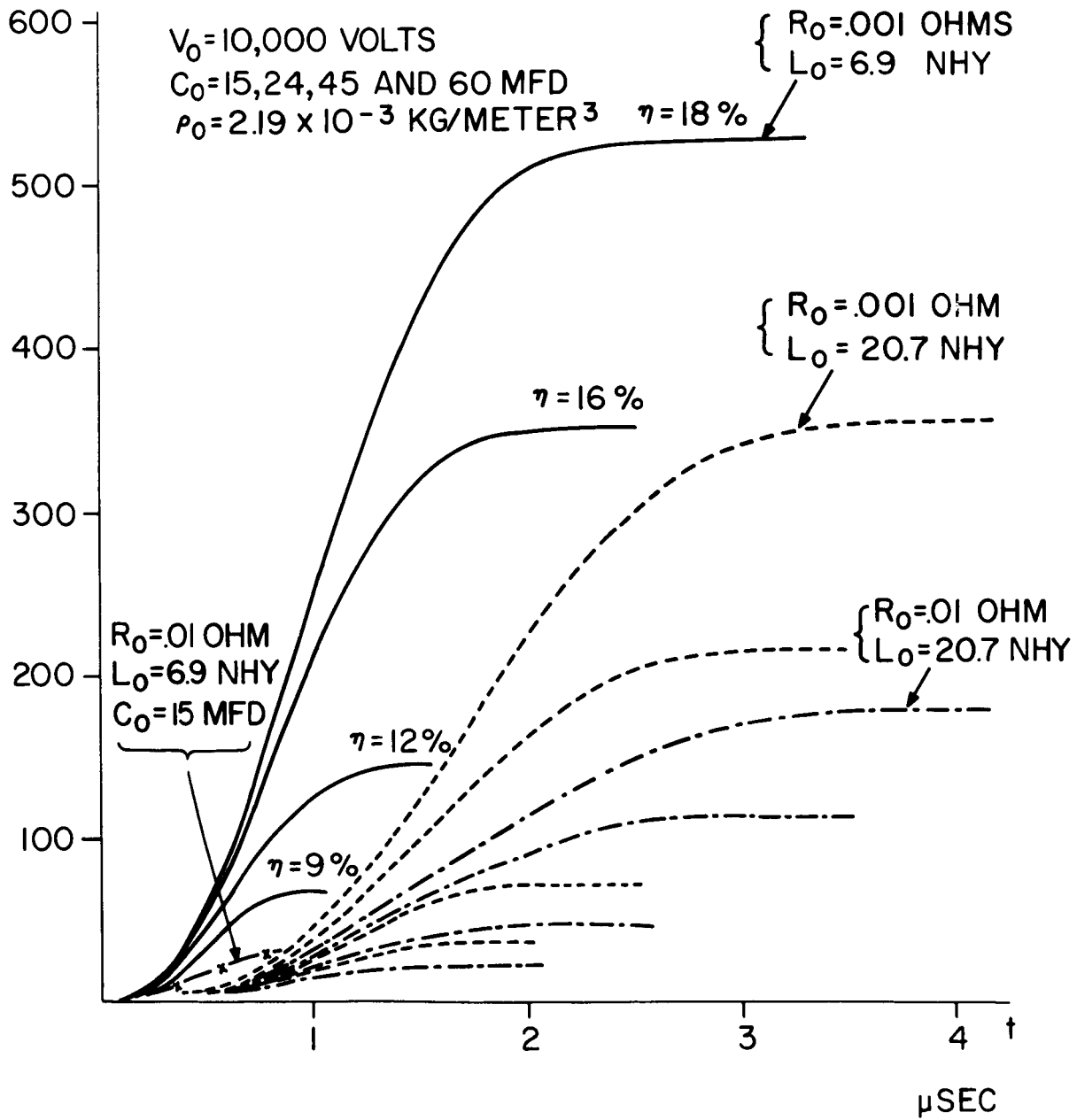
Figure 29. Variation of the Mechanical Energy with C_0 for Various Values of R_0 and L_0

E MECH (t)
IN JOULES

Co = 15 MFD

$V_o = 10,000$ VOLTS

$\rho_o = 2.19 \times 10^{-2}, 2.19 \times 10^{-3}, 2.19 \times 10^{-4},$
2.19×10^{5}, Kg/METERS

OR

$\rho_o = 1.9 \times 10^{-4}$

$V_o = 3.17, 10, 31.7, 100$ KV

$R_o = .001$ OHM
$L_o = 6.9$ NHY

$R_o = .01$ OHM
$L_o = 6.9$ NHY

$\eta = 10\%$

$R_o = .001$ OHM
$L_o = 20.7$ NHY

$R_o = .01$ OHM
$L_o = 20.7$ NHY
$\rho_o = 2.19 \times 10^{-4}$, Kg/m^3
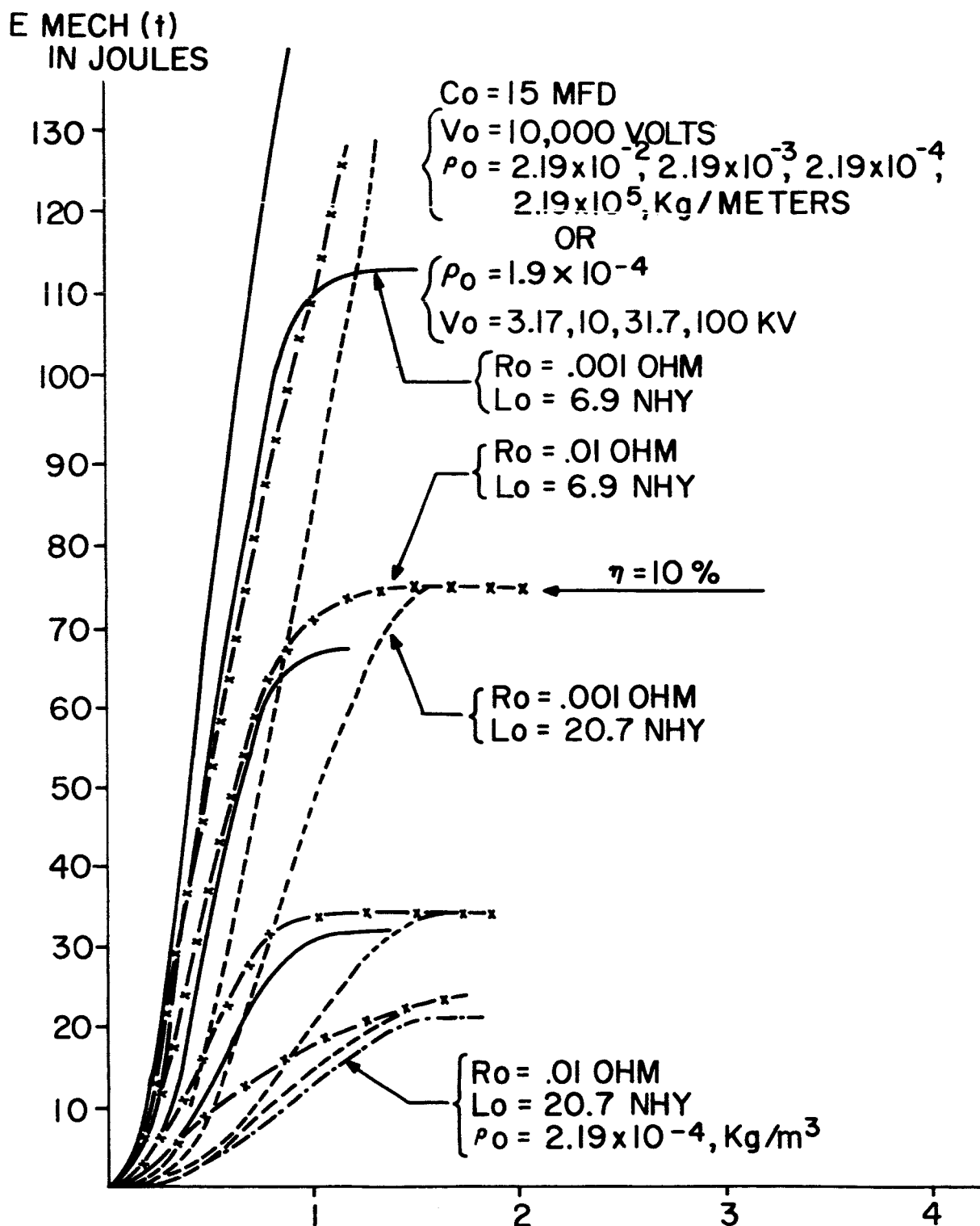
Figure 30. Variation of Mechanical Energy with ρ_o for Various Values
of R_o and L_o

83

the capacitance is increased, in the range studied. (Obviously, this trend cannot continue indefinitely.)

Another subtle trend shown by the $E(t)$ curves is the increase in efficiency by decreasing the breech density (ρ_o) or, increasing the initial voltage. Factors of ten decrease in density appear to double the efficiency, as do factors of $\sqrt{10}$ increase in voltage. One might mistakenly deduce the opposite trends by casual inspection of Equation (7.32). Obviously, ρ_o and V_o change the value of the integral more rapidly than V_o^2/ρ_o. The predicted trend in the efficiency with varying density has been qualitatively confirmed by casual observations made during the course of experimentation. The trend with voltage has been measured, and was found to follow the predicted trend. The experimental results are presented graphically in Figure 31.

The analysis would seem to indicate, then, that as high a voltage, as low a density, and as high a capacity as practical should be used for maximum efficiency, compatible with the desired I_{sp}. No limiting values for these variables were encountered in the few cases studied here. One might attempt predictions of trends outside the present range by contemplation of Equation (7.32), but to do so is difficult because of the complicated dependence of the value of the integral on each of the components of its coefficient. Qualitatively, the limit of

84
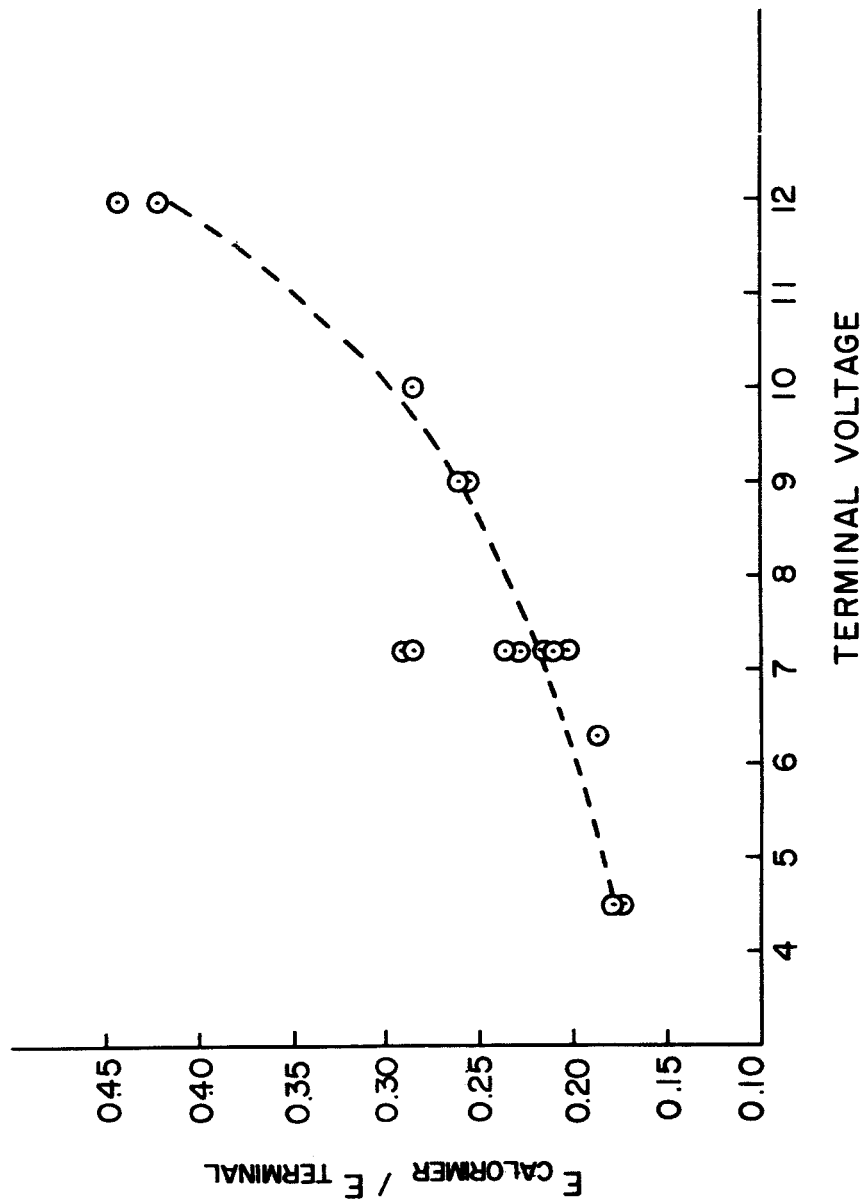
Figure 31. Calorimeter Energy/Thermal Energy vs Terminal Voltage
45 μf ~ 2nd Stage

85

the integral, t_2, seems to depend more on C_o than on V_o or $1/\rho_o$, and the peak value of the integrand seems to depend more on V_o and $1/\rho_o$ than it does on C_o. Both t_2 and $\dot{x}^3_{max}$ depend on the gun radii a and b, through L' and A.

7.6 Inadequacies of the Theory

Perhaps the most important omission in the theoretical model comes about as a result of the assumption that each particle encountered by the current sheet is ionized at least during the time in which that particle is in the sheet. (Subsequent recombination would not affect the results.) The omission referred to is a factor account for less than perfect ionization in the sheet, a factor which undoubtably depends on the potentials developed in the gun, particularly in the low voltage range. Such a factor would be important in determining the voltage dependence of the efficiency in the low voltage range.

This theory is also inadequate to describe those operating conditions under which the current sheet is observed not to be a single well-defined sheet, but is a narrow sheet followed by a broader current distribution, almost equal in amplitude to the current sheet itself.

A third serious inadequacy is the neglect of radial flow in the current sheet, as mentioned previously.

Another omission in the analysis has been an accounting of how the energy stored in the magnetic compression of the gas (in one dimension only) is released upon the decay of the magnetic field. As is shown later, the energy so stored is twice the mechanical energy, so that this

86

is an extremely important consideration. It might be conjectured that since the energy is stored in one-dimensional compression, it also will be released usefully in one-dimensional expansion. This point bears more careful analysis.

Other factors not taken into account are losses after passage of the current sheet such as randomizing collisions during (although hypothesized to be of second order here) and after the passage of the current sheet, ions gyrating into the electrode walls, the fact that particles accelerated during the first quarter cycle may overtake the current sheet on the second quarter cycle, (it should be noted that the deceleration of the current sheet in the second quarter cycle of current has never been observed experimentally, infact, most experimentalists report a constant current sheet velocity throughout the accelerating process) frictional losses due to too long a gun, and/or current bubble action in too short a gun. The last two of these factors may be qualitatively taken into account by intuitive arguments. An apparent experimental confirmation of the trends caused by the latter factors was indicated during the course of the thrust measurements. Using a 15 mfd capacitor, the thrust obtained with a 0.3 meter long electrode was a factor of about 2 greater than that obtained with a 0.5 meter electrode. With a 45 mfg capacitor, the trend was almost exactly reversed, i.e., the 0.55 meter electrode gave twice the thrust of the 0.30 meter electrode, all other conditions being equal.

Finally, the extent to which the assumption of a time-independent plasma resistance holds over the first half cycle of power is now known.

87

7.7 Distribution of the Energy in the Circuit

Equation (7.38) may be multiplied by $I(t)$ and integrated over t to give the following four terms, each of which represents a form of energy:

$$E_C = \frac{Q(t)}{2C_o} = \frac{1}{2C_o} \left(Q_o - \int_0^t I\,dt \right)^2 \qquad (7.40)$$

$$E_R = R \int_0^t I^2\,dt \qquad (7.41)$$

$$E_L = \frac{1}{2} L I^2 \qquad (7.42)$$

$$E_{electromech.} = \frac{L'}{2} \int_0^t I^2\,\dot{x}\,dt = \frac{2A}{3}\,\rho_o \int_0^t e^{-\frac{2x^2}{\ell_o^2}}\,\dot{x}^3\,dt$$

$$= 3E_{mech.} \qquad (7.43)$$

The last equality of Equation (7.43) was obtained by comparison with Equation (7.31). Since $E_{electromechanical}$ is the only source for work inside the gun, and since $E_{mechanical}$ is only one-third of $E_{electromechanical}$, the balance, $2/3\ E_{electromechanical}$, must be stored as potential energy, presumably in the magnetically compressed plasma in the gun. As was mentioned earlier, it is entirely possible that this potential energy may be converted to useful mechanical energy as the magnetic field inside the gun decays.

Evaluation of the integrals of Equations (7.40) to (7.43) at the time t_2 (the end of the 1st half-cycle of current) was carried out for the

following conditions:

$$V_O = 10,000 \text{ volts}$$

$$C_O = 15 \text{ mfd}$$

$$L_O = 6.9 \text{ nanohenries}$$

$$R_O = .001 \text{ ohm}$$

$$\rho_O = 2.19 \times 10^{-4} \text{ kg/m}^3$$

$$\ell_O = 0.2 \text{ m}$$

$$a = 1.9 \times 10^{-2} \text{ meter}$$

$$b = 3.8 \times 10^{-2} \text{ meter}$$

The results are:

$$E_C = 276 \text{ joules}$$

$$E_R = 54 \text{ joules}$$

$$E_L = 0$$

$$E_{Electromech} = \frac{337}{667}$$
$$\text{Total}$$

Taking into account the computational errors involved in the required graphical integrations, the total energy so determined is considered to be in good agreement with the total initial energy, 750 joules.

A computation of E_L at $t = t_1$ (first current peak) shows that $E_L(t_1) = 293$ joules so that $E(t_1) \approx E_c(t_2)$. Thus, most of the energy stored magnetically in L_O throughout the circuit at t_1 has been transferred back to the capacitor at t_2. The importance of

89

minimizing L_o is demonstrated by this computation. Although the energy similarly stored inside the active part of the gun, i.e. in L' $x(t_2)$, may also be transferred back to the capacitor, crow-barring techniques at the breech or, still better, designing for a critically damped circuit may serve to prevent such transfer and to permit utilization of this energy.

8. CONCLUSIONS AND SUMMARY

The primary effort of the work carried out during the contract period involved the study of the performance of the repetitively pulsed two-stage coaxial plasma engine. In order to provide the means for performing the necessary measurements, several useful instrumented facilities and techniques were developed and implemented. These have been described in some detail, together with a representative portion of the accumulated data. The data and the interpretations placed upon it constitute the basis for three general categories of information:

1. The operating characteristics of the major components of the existing engine system.

2. The trends in performance of the engine system with change of design and operating parameters.

3. The correlation of the experimental results to those predicted by an analytical model proposed for the description of the engine and its response to parametric changes.

Although we have treated all of these categories in the preceding sections, it would be well to summarize the factors which appear to

have the greatest influence on the achievement of optimum engine performance.

8.1 A Summary of Analytically Predicted and Experimentally Observed Trends

8.1.1 Circuit Inductance at $t = 0$

Prediction: A 3 x decrease in L_o gives a 1.5x - 1.9x increase in efficiency.

Observation: Qualitative agreement.

8.1.2 Circuit Resistance

Prediction: A 10x decrease in R_o gives a 3x increase in efficiency.

Observation: Not submitted to test.

8.1.3 Capacitance

Prediction: $\eta_2/\eta_1 \approx C_2/2C_1$

Observation: The trend was faster than $C_2 / 2C_1$, but L_o was decreased at the same time.

8.1.4 Density

Prediction: $\eta_2/\eta_1 \approx 1 + \log_{10} \dfrac{\rho_1}{\rho_2}$

(over the limited range studied only)

Observation: Qualitative trend informally noted.

8.1.5 Voltage

Prediction: $\eta_2/\eta_1 \approx 1 + 2 \log_{10} \dfrac{V_2}{V_1}$

(over the limited range studied only)

Observation: Good agreement with data of Figure 31.

91

8.1.6 Gun Length

Prediction: Not covered by the analysis, but trends can be qualitatively predicted by intuitive considerations of the losses incurred by wall collisions in too long a gun and "bubble" spreading in too short a gun.

Observation: Qualitative agreement.

8.1.7 Gas Pulse Shape:

Prediction: Included in the model, but computations were carried out for only one value of the characteristic length, ℓ_o, and one general shape (Gaussian).

Observation: Not submitted to test.

8.2 Areas for Immediate Improvement

The largest single loss factor in the plasma engine systems which we have investigated is that associated with the transfer of energy stored in the capacitor to the accelerator terminals. Over 65% of the energy initially stored in the capacitor bank is dissipated partially as a result of the stray inductances in the exterior circuit of the engine. It is reasonable to expect that an improvement of lead and capacitor design should greatly improve the transfer **efficiency.**

An immediate improvement in these conditions is planned for the next set of experiments by using capacitors of conventional, but improved design. Both the inductance and the equivalent series resistance ($\omega L/Q$) of these units have been quoted as approximately

50% lower than those for the units used in the present experiments. Still further improvement, by almost two orders of magnitude, is promised by the recent development of a more advanced design in capacitors with inductance in the fractional nanohenry range and Q in the 10^2 to 10^3 range. Such performance has been achieved by the use of improved foil and terminal lead configurations, and the substitution of dry mica sheet for the relatively high loss oil-paper dielectric. An additional advantage of the dry sandwich-like construction of these capacitors is that it should permit operation in a vacuum at elevated temperatures (100°C) without the difficulties which have been discussed previously.

Since it is suggested that these changes in inductance and equivalent series resistance may significantly improve energy transfer to the accelerator, it will be important to study the extent to which the resulting changes in the magnitude and time of rate change of voltage and current will effect energy transfer within the accelerator. It is obvious from the considerations discussed previously that optimum performance of the engine will be achieved only by appropriate matching of the electrical circuit characteristics to the geometrical characteristics of the accelerator and the density and distribution of the propellant load.

With respect to propellant loading, it seems probable that for the voltage and capacitance levels required for high accelerator efficiency, continuous propellant flow may be impractical. It has been shown that, depending on accelerator length and propellant molecular weight, pulsing rates as high as 1000 c.p.s. may be required for optimum utilization of a continuous flow of propellant through the engine. For typical operating values of 10 KV and 45 ufd, for example, a pulsing rate of 500 c.p.s. would require 1.1 megawatts of input power.

Operation at lower power levels, by utilizing proportionately lower firing rates at fixed values of V_O and C_O, introduces a necessity for the development of repetitively pulsed propellant injection devices. These devices must not only provide suitable timing and shaping of the gas load, but must also be reproducible in operation and, for space application, have long operating life and low power input requirement. Since the two-stage approach appears to be a feasible technique for ignition of the engine discharge at proper operating densities, several propellant pulsing techniques, either mechanical or fluid dynamic in nature, are under consideration for incorporation with the first stage of the engine system.

8.3 Additional Areas for Improvement

8.3.1 Electrode and Insulator Materials

The choice of suitable electrode materials must include considerations

94

of high initial conductivity, low temperature coefficient of resistance, and low sputtering rates with respect to the propellant species. Insulators should be designed primarily for maximum resistance to plating and to surface discharge.

From a long range view, preliminary tests have indicated that with sufficiently high pumping speed between the electrode flanges and with more efficient mass injections, it may be possible to entirely remove the interelectrode insulator from the discharge region.

8.3.2 Component Cooling

It has been demonstrated that increased electrode temperature with resultant increased circuit resistance may be a large energy dissipation factor in the engine performance. (The effects of resistance are demonstrated, for example, in the analytically obtained curves presented earlier in the report.)

Heating of capacitors is a parallel problem which may, in addition to effecting changes in circuit parameters, severaly curtail system life.

Although some effort has been devoted to conductive cooling of these components, studies should be extended to include the application of radiative cooling techniques.

8.3.3 Capacitor Charging

Resistor and inductor networks have been used for charging the

engine capacitor bank. For practical application, conventional RC circuit resistive charging may be ruled out on the basis of an inherent 50% dissipation of power in the resistance. The use of inductors in our present system has improved charging efficiency to over 90%, but it places a greater penalty on overall system weight. Charging circuits must be designed to provide an optimum match of engine firing rate requirements to the characteristics of the available power conditioning equipment.

8.3.4 Propellants

Although nitrogen, helium, hydrogen and argon have been used in the course of the above experimental program, it is apparent that additional fuels should be considered with respect to effects on electrode sputtering rates, engine operating stability and storage and handling. The use of solid fuel propellants that can be vaporized readily should also be studied.

8.4 Concluding Remarks

A few areas have been discussed which bear further investigation, primarily from the viewpoint of improving system efficiency and reliability. In the course of this experimental program, all of these, and several additional, areas have been examined at least briefly. To date, no indication has been found that any of the

problems encountered is insurmountable. The achievement of an accelerator efficiency of 43% is encouraging and neither the analytical nor the experimental results suggest that this represents an upper limit of accelerator performance. In the immediate future, research along the lines outlined will be aimed primarily at extending at least this level of performance to the overall engine system.

9. GENERAL ACKNOWLEDGMENTS

The authors wish to cite the continuing support of Joseph Farber in encouraging and facilitating the progress of these studies. Valuable experimental and analytical support was given by Mr. Gerard Brimmer and Mr. Stephen Collins, respectively.

REFERENCES

1. P. Gloersen, B. Gorowitz, and W. Palm, "Experimental
    Performance of a Pulsed Gas Entry Coaxial Plasma
    Accelerator, "Paper No. 1535-60 at the ARS 15th
    Annual Meeting, Washington, D. C., December 1960.

2. Per Gloersen, "Pulsed Plasma Accelerators", ARS Paper No. 2129-
    61, at the ARS Space Flight Report to the Nation in New
    York, October 1961.

3. B. Gorowitz, P. Gloersen, W. A. Hovis, Jr., "Experimental
    Studies of a Repetitively Fired Two-Stage Coaxial Plasma
    Engine, "Paper No. 2377-62 at the ARS Electric Propulsion'
    Conference, Berkeley, Calif., March 1962.

4. P. Gloersen, B. Gorowitz, W. A. Hovis, Jr., and R. B. Thomas, Jr.,
    "An Investigation of the Properties of a Repetitively Fired
    Two-Stage Coaxial Plasma Engine," Paper No. 5 at the
    Flight Application Session of the Third Symposium of the
    Engineering Aspects of MHD, Rochester, N.Y., March 1962.

5. R. F. Conner and J. Hyman, Jr., "Direct Thrust Measurement of
    Electrical Propulsion Devices, " ARS Paper No. 2180-61
    at ARS Space Flight Report to the Nation in New York,
    October 1961.

6. J. R. Anderson, S. L. Eilenberg, J. E. Etter, R. N. Olson,
    "Evaluation of Ion Engine Performance, " ARS Paper No.
    2185-61, at ARS Space Flight Report to the Nation in
    New York, October 1961.

7. C. F. Hendee and W. B. Brown, "Stroboscopic Operation of Photo-
    multiplier Tubes", Philips Technical Review 19, 50 (1957)

8. W. A. Hovis, Jr., "Time -resolved spectra of rare-earth ions, "
    J. Opt. Soc. Am. 52, 649-655 (1962)

9. L. D. Landau, E. M. Lifshitz, "Electrodynamics of Continuous
    Media," Addison-Wesley (1960).

10. L. C. Burkhardt and R. H. Lovberg, "The Current Sheet in a
    Coaxial Plasma Gun," Phys. Fluids 5, 341 (1962).

11. T. J. Gooding, B. R. Hayworth, and R. H. Lovberg, "Development
    of a Coaxial Plasma Gun for Space Propulsion, " Final Report No.
    GDA 63-0454 (NASA/General Dynamics Contract NAS 3-2501) (May 1963).

SUMMARY REPORT DISTRIBUTION LIST

CONTRACT NAS3-2502

Address	Number of Copies
1. National Aeronautics and Space Administration 1512 H Street Washington, D. C. 20546 Attn: I. R. Schwartz (RNT)	3
2. NASA, Langley Research Center Langley Field, Virginia 23365 Attn: M. Ellis	2
3. NASA, Marshall Space Flight Center Huntsville, Alabama 35812 Attn: E. Stuhlinger (M-RP-DIR)	1
4. NASA, Ames Research Center Moffet Field, California 94035 Attn: Dr. G. Goodwin	1
5. Jet Propulsion Laboratory 4800 Oak Grove Drive Pasadena, California Attn: J. J. Paulson	1
6. Aeronautical Systems Division Wright-Patterson Air Force Base, Ohio 45433 Attn: ASRMPE, R. Supp.	2
7. Headquarters, USAF Air Force Office of Scientific Research Washington, D. C. 20546 Attn: Dr. M. Slawsky	1
8. General Electric Company Missile and Space Division Valley Forge Space Technology Center P. O. Box 8555 Philadelphia 1, Pennsylvania Attn: Dr. P. Gloersen	1
9. Magnetohydrodynamics, Inc. P. O. Box 1815 Newport Beach, California Attn: Dr. V. Blackman	1

Address	Number of Copies
10. Electro-Optical Systems, Inc. 125 N. Vinedo Avenue Pasadena, California Attn: Dr. T. M. Teem	1
11. Aerospace Corporation P. O. Box 95085 Los Angeles 45, California Attn: Dr. H. Mirels Library Technical Documents Group	2
12. AVCO - Everett Research Laboratory Everett, Massachusetts Attn: Dr. A. R. Kantrowitz	1
13. Aeronutronics - Ford Motor Company Newport Beach, California Attn: Dr. S. R. Byron	1
14. Plasmadyne Corporation 3839 South Main Street Santa Ana, California Attn: Dr. M. C. Gourdine	1
15. Northrop Corporation 1111 East Broadway Hawthorne, California Attn: P. Lenn	1
16. Allison Division, GMC Indianapolis, Indiana Attn: T. L. Rosebrock	1
17. Litton Systems, Inc. Beverly Hills, California Attn: A. S. Penfold	1
18. Radio Corporation of America Astro-Electronics Division Princeton, New Jersey Attn: T. T. Reboul	1
19. Republic Aviation Corporation Plasma Propulsion Laboratory Farmingdale, Long Island, New York Attn: A. E. Kunen	1

Address	Number of Copies

20. Space Technology Laboratory
    One Space Park
    Redondo Beach, California
    Attn: Dr. C. L. Dailey
    — 1

21. United Aircraft Corporation
    Research Laboratories
    East Hartford 8, Connecticut
    Attn: R. G. Meyerand
    — 1

22. TAPCO A Division of
    Thompson Ramo Wooldridge, Inc.
    7209 Platt Avenue
    Cleveland, Ohio 44104
    Attn: R. T. Craig
    — 1

23. Rocketdyne
    6633 Canoga Avenue
    Canoga Park, California
    Attn: Dr. R. H. Boden
    — 1

24. Space Dynamics Corporation
    2215 Florence Avenue
    Cincinnati 6, Ohio
    Attn: M. L. Ghai
    — 1

25. Unified Science Associates, Inc.
    826 Sourth Arroyo Parkway
    Pasadena, California
    Attn: S. Naiditch
    — 1

26. Rocket Research Corporation
    233 S. Holden Street
    Seattle 8, Washington
    Attn: M. E. Maes
    — 1

27. Lockheed Missile Systems Division
    Palo Alto, California
    Attn: D. Bershader
    — 1

28. Graduate School of Aeronautical Engineering
    Cornell University
    Ithaca, New York
    Attn: Professor E. L. Resler, Jr.
    — 1

29. Cast Institute of Technology 10900 Euclid Avenue Cleveland, Ohio 44106 Attn: Professor O. K. Mawardi	1
30. Massachusetts Institute of Technology Naval Supersonic Laboratory Cambridge, Massachusetts Attn: T. K. Kerrebrock and E. E. Covert	1
31. Rensselaer Polytechnic Institute Troy, New York Attn: Dr. E. H. Holt	1
32. NASA, Lewis Research Center Spacecraft Technology Division 21000 Brookpark Road Cleveland, Ohio 44135 Attn: J. H. Childs	3
33. NASA, Lewis Research Center Electromagnetic Propulsion Division 21000 Brookpark Road Cleveland, Ohio 44135 Attn: G. Seikel	1
34. NASA, Lewis Research Center Electromagnetic Propulsion Division 21000 Brookpark Road Cleveland, Ohio 44135 Attn: W. E. Moeckel	1
35. NASA, Lewis Research Center Electromagnetic Propulsion Division 21000 Brookpark Road Cleveland, Ohio 44135 Attn: E. Reshotko	1
36. NASA, Lewis Research Center 21000 Brookpark Road Cleveland, Ohio 44135 Attn: Library	1

Address	Number of Copies

37. NASA, Lewis Research Center   1
    Office of Patent Counsel
    21000 Brookpark Road
    Cleveland, Ohio 44135
    Attn: N. T. Musial

38. NASA, Lewis Research Center   1
    Spacecraft Technology Procurement Section
    21000 Brookpark Road
    Cleveland, Ohio 44135
    Attn: John H. DeFord

39. NASA, Lewis Research Center   2
    Spacecraft Technology Division
    21000 Brookpark Road
    Cleveland, Ohio 44135
    Attn: Peter Ramins

40. John A. Satkowski   1
    Office of Naval Research
    Washington 25, D. C.

41. General Dynamics/Astronautics   1
    San Diego 12, California
    Attn: Dr. T. Gooding and Dr. R. H. Lovberg

42. Clauser Technology Corporation   1
    3510 Torrance Boulevard
    Torrance, California
    Attn: Dr. M. Clauser

43. The Marquardt Corporation   1
    16555 Saticoy Street
    Van Nuys, California
    Attn: A. N. Thomas

44. Detachment 4, ASR (ASQWR)   1
    Eglin AFB, Florida
    Attn: Lt. C. F. Ellis

45. NASA, Scientific and Technical Information Facility   2 + a reproducible
    Box 5700
    Bethesda 14, Maryland
    Attn: NASA Representative RQT-2448

Address	Number of Copies

46. Westinghouse Astronuclear Laboratories   1
    Pittsburgh 34, Pennsylvania
    Attn: Mr. H. W. Syzmanowski, Manager
        Electrical Propulsion Laboratory

47. Space Sciences Incorporated   1
    301 Bear Hill Road
    Waltham, Massachusetts 02154